Precision Measurement of Parity-violation in Deep Inelastic Scattering Over a Broad Kinematic Range

Addendum for PAC35

December 14, 2009

Abstract

We propose to measure the parity-violating electroweak asymmetry A_{PV} in the deep-inelastic scattering of polarized electrons (PVDIS) to high precision in order to search for physics beyond the Standard Model in lepton-quark neutral current interactions. As described in the original document (proposal E09-012), the proposed measurement is unique in that it is sensitive to axial hadronic weak neutral currents. The Standard Model predictions for the corresponding weak neutral current coupling constants have not been tested with a high degree of precision. A comprehensive search for physics beyond the Standard Model requires precise measurements of all leptonic and semi-leptonic coupling constants as a complement to direct searches at the Large Hadron Collider. Deep inelastic scattering with a moderately high energy beam and high luminosity as well as a spectrometer with a broad kinematic is required. The original proposal document describes how the required sensitivity becomes feasible with a solenoidal spectrometer and a 11 GeV beam.

In this document, we further elaborate on hadronic physics issues that could potentially cloud the interpretation of the results in terms of electroweak parameters. The hadronic physics topics addressed and the associated potential auxiliary measurements are interesting in their own right. The search for parton-level charge symmetry violation and a precise measurement of the d/u ratio were already addressed in the original proposal. We expand on recent theoretical input that reinforces our original statements on the unique nature of the hadron dynamics that become manifest from potentially precise measurements of higher-twist effects. It is thus feasible to simultaneously probe for physics beyond the standard model, constrain or measure novel and dynamically interesting higher twist effects, and search for charge symmetry violation at high x.

The original proposal described the experimental strategy to obtain large acceptance by using a superconducting solenoidal magnet. We have carried out preliminary studies of a conceptual engineering design of the proposed spectrometer choice and find that it is feasible to mount and dismount the experimental apparatus in the solenoid with relative ease, making it possible to interleave physics runs of the proposed experiment with other approved projects in Hall A.

P. Bosted, J. P. Chen, E. Chudakov, A. Deur, O. Hansen, C. W. de Jager, D. Gaskell, J. Gomez, D. Higinbotham, J. LeRose, R. Michaels, S. Nanda, A. Saha, V. Sulkosky, and B. Wojtsekhowski
Jefferson Lab, Newport News, VA 23606

P. A. Souder (*Contact**) and R. Holmes
Syracuse University, Syracuse, NY 13244

K. Kumar, D. McNulty, L. Mercado, and R. Miskimen
University of Massachusetts Amherst, Amherst, MA 01003

H. Baghdasaryan, G. D. Cates, D. Crabb, M. Dalton, D. Day, N. Kalantarians, N. Liyanage, V. V. Nelyubin, B. Norum, K. Paschke, S. Riordan, O. A. Rondon, M. Shabestari, J. Singh, R. Subedi, A. Tobias, K. Wang, and X. Zheng
University of Virginia, Charlottesville, VA 22904

J. Arrington, K. Hafidi, P. E. Reimer, and P. Solvignon
Argonne National Laboratory, Argonne, IL 60439

D. Armstrong, and T. Averett
College of William and Mary, Williamsburg, VA 23173

P. Decowski
Smith College, Northampton, MA 01063

L. El Fassi, R. Gilman, R. Ransome, and E. Schulte
Rutgers, The State University of New Jersey, Piscataway, NJ 08855

W. Chen, H. Gao, M. Huang, G. Laskaris, X. Qian, Y. Qiang, Q.J. Ye, and Q. Ye
Duke University, Durham, NC 27708

K. A. Aniol
California State University, Los Angeles, CA 90032

F. Meddi and G. M. Urciuoli
Dipartimento di Fisica dell Università La Sapienza INFN, Sezione di Roma, I-00185 Roma, Italy

A. Lukhanin, Z. E. Meziani, and B. Sawatzky
Temple University, Philadelphia, PA 19122

P. M. King and J. Roche
Ohio University, Athens, OH 45701

E. Beise
University of Maryland, College Park, MD 20742

W. Bertozzi, S. Gilad, W. Deconinck, S. Kowalski, and B. Moffit
Massachusetts Institute of Technology, Cambridge, MA 02139

F. Benmokhtar, G. Franklin, B. Quinn
Carnegie Mellon University, Pittsburgh, PA 15213

G. Ron
Tel Aviv University, Tel Aviv, Israel 69978

T. Holmstrom
Longwood University, Farmville, VA 23909

P. Markowitz
Florida International University, Miami, FL 33199

X. Jiang
Los Alamos National Laboratory, Los Alamos, NM 87544

W. Korsch
University of Kentucky, Lexington, KY 40506

J. Erler
Universidad Autónoma de México, 01000 México D. F., México

M. J. Ramsey-Musolf
University of Wisconsin, Madison, WI 53706

C. Keppel
Hampton University, Hampton, VA 23668

H. Lu, X. Yan, Y. Ye, and P. Zhu
University of Science and Technology of China, Hafei, 230026, P. R. China

N. Morgan and M. Pitt
Virginia Tech, Blacksburg, VA 24061

J.-C. Peng
University of Illinois, Urbana-Champaign, IL 61820

H. P. Cheng, R. C. Liu, H. J. Lu, and Y. Shi
Institute of Applied Physics, Huangshan University, Huangshan, P. R. China

S. Choi, Ho. Kang, Hy. Kang, B. Lee, and Y. Oh
Seoul National University, Seoul 151-747, Korea

J. Dunne and D. Dutta
Mississippi State University, Mississippi State, MS 39762

K. Grimm, K. Johnston, N. Simicevic, and S. Wells
Louisiana Tech University, Ruston, LA 71272

O. Glamazdin and R. Pomatsalyuk
NSC Kharkov Institute for Physics and Technology, Kharkov 61108, Ukraine

Z. G. Xiao
Tsinghua University, Beijing, P. R. China

B.-Q. Ma and Y. J. Mao
School of Physics, Beijing University, Beijing, P. R. China

X. M. Li, J. Luan, and S. Zhou
China Institute of Atomic Energy, Beijing, P. R. China

B. T. Hu, Y. W. Zhang, and Y. Zhang
Lanzhou University, Lanzhou, P. R. China

C. M. Camacho, E. Fuchey, C. Hyde and F. Itard
LPC Clermont, Université Blaise Pascal CNRS/IN2P3 F-63177 Aubière, France

A. Deshpande
SUNY Stony Brook, Stony Brook, NY 11794

A. T. Katramatou and G. G. Petratos
Kent State University, Kent, OH 44242

J. W. Martin
University of Winnipeg, Winnipeg, MB R3B 2E9, Canada

E. Cisbani, S. Frullani and F. Garibaldi
INFN, Gruppo Collegato Sanità and Istituto Superiore di Sanità, I-00161 Rome, Italy

M. Capogni
Istituto Nazionale di Metrologia delle Radiazioni Ionizzanti ENEA, and INFN - Gruppo Collegato Sanità, I-00161 Rome, Italy

V. Bellini, A. Giusa, F. Mammoliti, G. Russo and M.L. Sperduto
INFN Sezione di Catania and Dipartimento di Fisica e Astronomia, Università di Catania, I-95123 Catania, Italy

C.M. Sutera
INFN Sezione di Catania and Università di Catania, I-95123 Catania, Italy

* e-mail: souder@physics.syr.edu

Contents

Chapter 1

Introduction

This Addendum to the proposal E09-012 [1] is prepared for PAC35 in order to answer the questions from PAC34.

We reiterate here the physics topics that become accessible with the advent of a longitudinally polarized 11 GeV electron beam via measurements of the parity-violating asymmetry A_{PV} in deep inelastic scattering (DIS) in the kinematic region of large Bjorken $x = Q^2/2M\nu$. A_{PV} is defined to be:

$$A_{PV} = \frac{\sigma_R - \sigma_L}{\sigma_R + \sigma_L} \tag{1.1}$$

where $\sigma_R(\sigma_L)$ is the cross-section for incident right-(left-) handed electrons. With the proposed data set over a broad kinematic range that can be obtained simultaneously, we are able to:

1. Search for new interactions beyond the Standard Model (SM) in a unique way. The special feature of PVDIS is that it is sensitive to axial-hadronic currents, yet is insensitive to unknown radiative corrections that cloud the interpretation of lower energy experiments sensitive to these currents.

2. Search for Charge Symmetry violation (CSV) at the quark level.

3. Search for higher-twist effects in the parity-violating asymmetry. Significant higher-twist effects are observed in DIS cross sections, but in PVDIS large higher-twist contributions can only be due to quark-quark correlations.

4. Measure the d/u ratio in the proton, without requiring any nuclear corrections.

5. Determine if additional CSV is induced in heavier nuclei. Such an effect would have profound implications for our understanding of the EMC effect.

The unique opportunities for experiments on parity-violation at Jlab with the 11 GeV upgrade were recognized in the NSAC long-range planning exercises and elaborated on in the original proposal. That document also contained a full discussion of the physics

motivation, which we reiterate here in Chapter 2. In addition in the same chapter, we have a more complete discussion of the dynamics of higher-twist effects in deep inelastic scattering, using the input from a theory workshop that took place in Wisconsin in June 2009. Then in Chapter 3, we describe a concept for assembling and dismounting the experimental apparatus inside a large solenoid so as to make interleaving of other major experiments possible in Hall A. We conclude in Chapter 4 with an update on collaboration issues, cost estimates and assignment of tasks.

Chapter 2

Motivation

2.1 Parity Violation in DIS

2.1.1 Introduction

In the following, we reintroduce the formalism and summarize the primary physics motivation, which is to search for electroweak physics beyond the Standard Model at the TeV scale, before outlining the interesting hadronic physics that can also be simultaneously accessed. The parity-violating part of the semi-leptonic weak neutral current amplitude A_Z, denoted $\tilde{A}_Z$, can be isolated by the technique of measuring the helicity-dependent asymmetry

$$-A_{LR} = A_{PV} = \frac{\sigma_R - \sigma_L}{\sigma_R + \sigma_L} \sim \frac{\tilde{A}_Z}{A_\gamma} \sim \frac{G_F Q^2}{4\pi\alpha}(g_A^e g_V^T + \beta g_V^e g_A^T) \tag{2.1}$$

Here β is a kinematic-dependent factor that tends to be large for large scattering angles in the center-of-momentum frame. For the Standard Model, $g_A^e = 1$ is large, whereas $g_V^e = -1 + 4\sin^2\theta_W$ is small[1].

A notable gap in published measurements in searches for parity-violating extensions of the Standard Model [3, 4, 5, 6] is a precise test of the prediction for hadronic axial-vector currents, the term with g_A^T in Equation 2.1. The main reason, best known in the case of elastic nucleon scattering, is that the electroweak radiative corrections often have large uncertainties involving anapole moments or box diagrams containing more than one quark [7, 8]. Thus a precise measurement, even at the appropriate kinematics, would be dominated by theoretical errors. The one exception is deep inelastic scattering (DIS). Since in this case the scattering is from isolated elementary quarks, all radiative corrections are calculable. With the advent of the 11 GeV upgrade, significant phase space for DIS measurements becomes available.

In light of the high proposed precision, we have comprehensively investigated hadronic corrections that might be significant. The corrections are smallest for isoscalar targets

[1]Here we are using the conventions from Hobbs and Melnitchouk [2], which are different from those used by the PDG.

like deuterium. Even in deuterium, however, there are two interesting effects given the precision that we hope to reach with the proposed apparatus:

1. Charge symmetry violation (CSV) at the quark level. Present limits on the assumption that the up quark distribution in the proton is the same as the down quark distribution in the neutron are not sufficient for our proposed precision.

2. Finite Q^2 effects. Such effects are significant in the cross sections for $x > 0.5$, but it is not known whether or not they cancel in the asymmetry. If they do not cancel, they provide direct evidence for quark-quark correlations in the nucleon.

We find that these hadronic effects are extremely interesting in themselves.

2.1.2 PVDIS in the Quark-Parton Model

At JLab energies, the interactions of the Z-boson and heavier particles can be approximated by four-fermion contact interactions. The parity-violating part of the electron-hadron interaction can then be given in terms of phenomenological couplings C_{ij}

$$\mathcal{L}^{PV} = \frac{G_F}{\sqrt{2}}[\overline{e}\gamma^\mu\gamma_5 e(C_{1u}\overline{u}\gamma_\mu u + C_{1d}\overline{d}\gamma_\mu d) + \overline{e}\gamma^\mu e(C_{2u}\overline{u}\gamma_\mu\gamma_5 u + C_{2d}\overline{d}\gamma_\mu\gamma_5 d)]$$

with additional terms as required for the heavy quarks. Here C_{1j} (C_{2j}) gives the vector (axial-vector) coupling to the j^{th} quark.

The cross sections for DIS can be expressed in terms of structure functions $F_i^j(x, Q^2)$, as discussed in detail in Appendix B.2. Apart from the two electromagnetic structure functions F_1^γ and F_2^γ, for PVDIS three more structure functions: $F_1^{\gamma Z}$, $F_2^{\gamma Z}$ and $F_3^{\gamma Z}$. The axial-vector hadronic current is described by $F_3^{\gamma Z}$. The relative weighting of the different structure functions is a function of the kinematic variable $y \equiv \nu/E$, where ν is the energy loss in the lab frame.

In the limit of large Q^2, the structure functions can be described by parton distribution functions (PDFs) $f_i(x)$ ($\overline{f}_i(x)$), which are the probabilities that the i^{th} quark (antiquark) carries a fraction x of the nucleon momentum. In this limit, the structure functions have a logarithmic Q^2-dependence given by QCD evolution. With the definitions $f_i^\pm = f_i \pm \overline{f}_i$, $y = \nu/E$, the asymmetry can be written

$$A_{PV} = -\frac{G_F Q^2}{4\sqrt{2}\pi\alpha}\left[Y_1 a_1(x) + Y_3(y) a_3(x)\right] \tag{2.2}$$

where

$$Y_1 \approx 1; \quad Y_3 \approx \frac{1-(1-y)^2}{1+(1-y)^2} \equiv f(y) \tag{2.3}$$

and

$$a_1(x) = g_A^e \frac{F_1^{\gamma Z}}{F_1^\gamma} = 2\frac{\sum_i C_{1i} Q_i f_i^+(x)}{\sum_i Q_i^2 f_i^+(x)}; \quad a_3(x) = \frac{g_V^e}{2}\frac{F_3^{\gamma Z}}{F_1^\gamma} = 2\frac{\sum_i C_{2i} Q_i f_i^-(x)}{\sum_i Q_i^2 f_i^+(x)}$$

2.2 Precision Electroweak Physics with Deuterium

For isoscalar targets such as the deuteron, the structure functions cancel and we have

$$a_1^D(x) = \frac{6}{5}(2C_{1u} - C_{1d})\left(1 + \frac{0.6s^+}{u^+ + d^+}\right); \quad a_3^D(x) = \frac{6}{5}(2C_{2u} - C_{2d})\left(\frac{u^- + d^-}{u^+ + d^+}\right) + \ldots \quad (2.4)$$

For $x > 0.4$, only valence quarks are important, and the expressions for a_1 and a_3 become constants. Then the asymmetry becomes

$$A_{PV}^D = -\frac{G_F Q^2}{\sqrt{2}\pi\alpha}\left(\frac{9}{20}\right)\left[1 - \frac{20}{9}\sin^2\theta_W + (1 - 4\sin^2\theta_W) f(y)\right]. \quad (2.5)$$

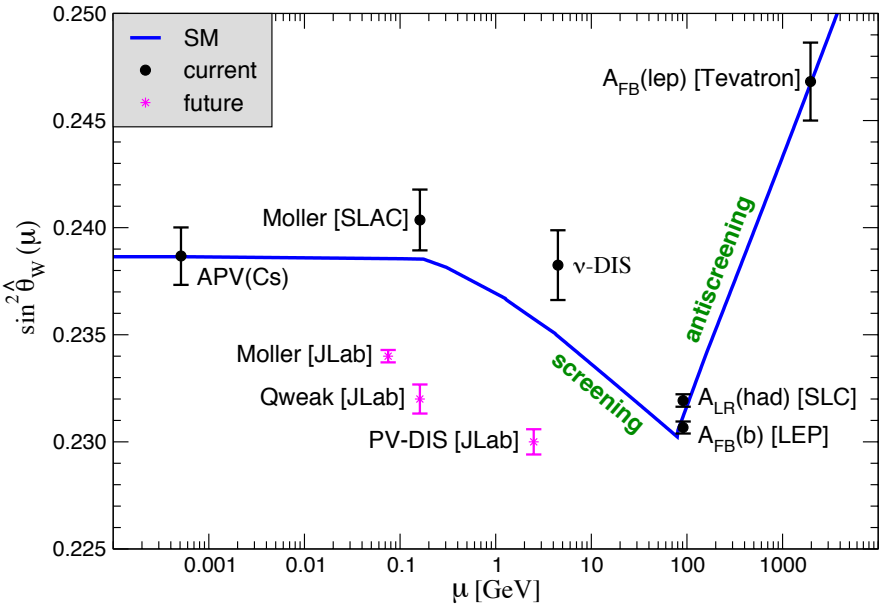

Figure 2.1: Plot of $\sin^2\theta_W$ versus Q for various precision experiments that are either completed or proposed.

One goal of PVDIS is to search for new physics beyond the Standard Model. With that in mind, we have designed the experiment so that we can obtain a precision of 0.6% on the combination of electroweak parameters in A_{PV}^D, as described in Section 2.4.3 below. One signature for the new physics is a deviation of the value of $\sin^2\theta_W$ obtained from comparing the data with Equation 2.5. The resulting sensitivity for our projected error is plotted in Figure 2.1, together with the results of other precise measurements, both published and proposed.

From a more phenomenological perspective, a measurement of A_{PV}^D provides a limit on deviations of the couplings C_{ij} from the predictions of the Standard Model. The

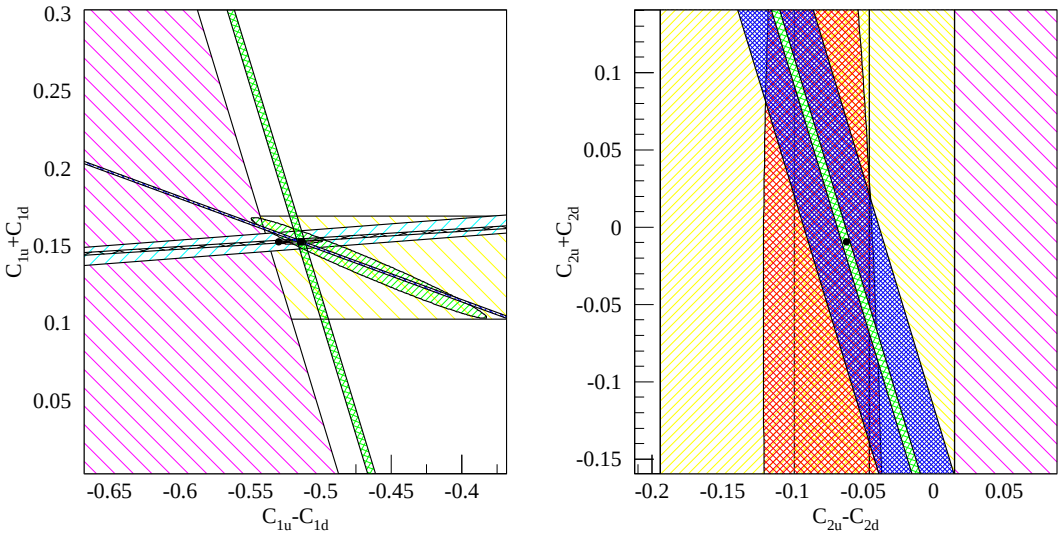

Figure 2.2: Constraints on the Standard Model from parity-violation experiments. The magenta/yellow hatched bands present the SLAC-DIS/Bates results. The cyan/black hatched band presents the Tl/Cs APV result. The narrow black band in the left plot shows the expected results from Qweak. The red band in the right plot shows the PDG constraint, and the blue band shows the expected precision from the approved 6 GeV PVDIS experiment (E08-011) [9] which will run in 2009. The green bands show the expected results from the experiment proposed. All limits are 1 standard deviation.

resulting sensitivity on plots of the C_{ij}'s is given in Figures 2.2 and 2.3. There is a tremendous decrease in the allowed region of the C_2 plot. Both the high statistical sensitivity and the large values of Y_3 due to the large scattering angles are important for this improvement. The unique feature of PVDIS is that it provides a precise constraint in the plot of the C_2's.

As discussed in a recent review by Ramsey-Musolf and Su [10], combining various precision measurements at low energies can have an important impact on physics beyond the Standard Model. In this spirit, these data will be complementary to the anticipated high-energy data from the LHC. PVDIS is one example of these low-energy experiments [11].

2.2.1 Contact Interactions

A general, model-independent way to parametrize the contributions of contact interactions of high-mass particles to low-energy measurements is to use the Lagrangian

$$\mathcal{L}_{eq} = \sum_{i,j=L,R} \frac{g_{ij}^2}{\Lambda^2} \, \overline{e}_i \gamma_\mu e_i \, \overline{q}_j \gamma^\mu q_j \tag{2.6}$$

Here $e_{L/R} = \frac{1}{2}(1 \mp \gamma_5)\psi_e$ and $q_{L/R} = \frac{1}{2}(1 \mp \gamma_5)\psi_q$ are the chirality projections of the fermion spinors, the g_{ij} are the coupling constants $g_{ij} = 2g_{ij}^u - g_{ij}^d$ and Λ is the mass

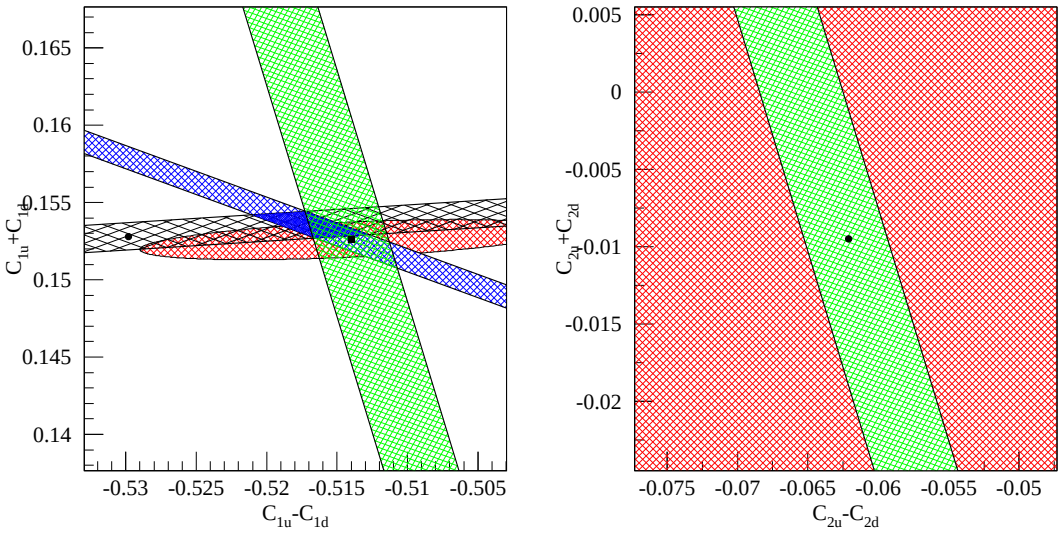

Figure 2.3: Expanded view of constraints on the Standard Model from parity-violation experiments (Fig. 2.2). The black crossed band presents the Cs APV results, the blue band - the expected QWEAK result, the red ellipse is a PDG fit, the black dots indicate the SM expectation and the best PDG fit, while the green band shows the current proposal. The anticipated error band from the future E08-011 experiment would also fill the entire region visible in the right plot. All limits are 1 standard deviation.

scale.

The projected results on A_{PV}^{D} translates into a measurement of the linear combination of the phenomenological couplings $2\left[(2C_{1u}-C_{1d})-0.84\,(2C_{2u}-C_{2d})\right]$ to an accuracy of ± 0.0098. This translates into

$$\frac{\Lambda}{\sqrt{|g_{RR}^2-g_{LL}^2+g_{RL}^2-g_{LR}^2|}}=\frac{1}{\sqrt{\sqrt{2}G_F|0.0098|}}\simeq 2.5\text{ TeV}. \tag{2.7}$$

For example, models of lepton compositeness are characterized by strong coupling dynamics. Taking $\sqrt{|g_{RR}^2-g_{LL}^2+g_{RL}^2-g_{LR}^2|}=2\pi$ shows that mass scales as large as $\Lambda=15.5$ TeV can be probed, corresponding to electron and quark substructure at the level of $\sim 10^{-20}$ m.

There are two kinds of new interactions that can contribute to PVDIS. One is the contact interactions mentioned above, which can include particles such as extra Z-bosons, leptoquarks, and supersymmetric (SUSY) partners. Contact interactions have real amplitudes, so they do not interfere with the imaginary amplitudes measured on the Z-pole at LEP and SLAC. Hence low energy measurements are competitive. In addition, the new generation of experiments at JLab, including Qweak, PVDIS, and Møller, has the precision to probe contributions to radiative corrections from loops involving new particles that do not directly couple to quarks and leptons.

Z' Bosons

A specific example of the kind of new physics to which the proposed experiment may be sensitive to are extra neutral gauge (Z') bosons with masses, $M_{Z'}$, in the TeV region. While these are very well motivated in many (if not most) models of physics beyond the SM, they are in general severely constrained by atomic parity violation (APV) measurements in Cs (and Tl) which agree with the SM prediction. However, APV in heavy nuclei is sensitive roughly to the sum of up and down quark vector couplings, and is thus blind to models where these are of similar size but opposite sign.

An example is the case where only right-handed quarks and leptons are charged under the underlying extra $U(1)'$ gauge factor[2] with charges proportional to the third component of the $SU(2)_R$ gauge group appearing in left-right symmetric models (it is not actually necessary that the $U(1)'$ is promoted to $SU(2)_R$). This case is interesting since the current precision electroweak data can accommodate such a heavy Z' with a mass as small as 660 GeV. If this case was actually realized in nature, the proposed measurement would see a 4σ deviation from the Standard Model prediction. For this particular example, the sensitivity of this proposal exceeds that of any other low-energy parity-violation measurement in the electron-quark sector.

Supersymmetry

Another good example of new physics contributing to A_{PV} is in the case of SUSY. Predictions for the contributions of SUSY to both PVDIS and Qweak for models of supersymmetry (SUSY) are shown in Fig. 2.4. There are two classes of models shown, one that conserves R-parity and one that does not. For R-parity conserving models, where the effects are confined to loops, PVDIS is a bit more sensitive, but the predictions are highly correlated. For the R-parity-violating case, where contact interactions are important, the predictions for the two experiments are totally uncorrelated. If SUSY were observed at the LHC and the result from PVDIS were below the prediction, the implication would be that SUSY violates R-parity, which in turn implies that the lightest SUSY particle is unstable and is not a good candidate for dark matter.

2.3 Hadron Physics with Deuterium

2.3.1 Charge Symmetry Violation

One critical assumption for the cancellation of the structure functions in A_{PV} for the deuteron is charge symmetry, namely $u^p = d^n$ and $u^n = d^p$. Charge symmetry violation (CSV) can be parametrized by new PDFs

$$\delta u \equiv u^p - d^n; \quad \delta d \equiv d^p - u^n; \quad R^{CSV} \equiv \frac{\delta u - \delta d}{u + v}$$

[2]For instance, a model of this type can be obtained from an E_6 gauge group when large kinetic mixing with the hypercharge boson is induced.

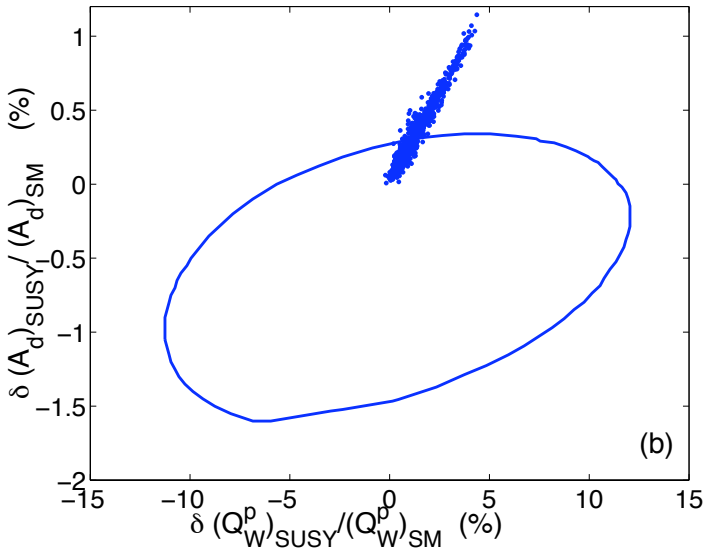

Figure 2.4: Implications of a measurement of PVDIS and Qweak for SUSY models. Dots: typical models for the R-parity conserving case. Line: region allowed at the 95% confidence level for models that violate R-parity but are consistent with other existing electroweak data.

Although the δu and δd are small, the ratio R^{CSV} can be significant if these CSV PDFs drop more slowly than the valence u and d with increasing x. There is no direct evidence for CSV at the parton level [12]. However, our PVDIS data will be more sensitive to CSV than any previous data, so we can set the best limits at large values of x.

There is some indirect evidence for CSV in neutrino scattering [13,14]. The Paschos-Wolfenstein ratio

$$R^{PW} = \frac{\sigma\langle \nu N \to \nu X\rangle - \sigma\langle \overline{\nu} N \to \overline{\nu} X\rangle}{\sigma\langle \nu N \to \mu X\rangle - \sigma\langle \overline{\nu} N \to \overline{\mu} X\rangle} \sim \frac{1}{2} - \sin^2\theta_W$$

which has been precisely measured by the NuTeV collaboration [15], is quite sensitive to CSV. In particular,

$$\frac{\delta R^{PW}}{R^{PW}} \sim 0.85 R^{CSV}$$

The discrepancy of the NuTeV result with the Standard Model expectation may indeed be due to CSV.

As a consequence of the above, the MRST group inserted CSV-violating terms to their global fits [16] and found that sufficient CSV is allowed to account for the NuTeV result. Non-zero values of R^{CSV} have been suggested in the literature caused both by non-perturbative QCD effects [17,18] as well as QED effects in the Q^2 evolution [19,20]. These are also in the range that would be significant for the NuTeV result.

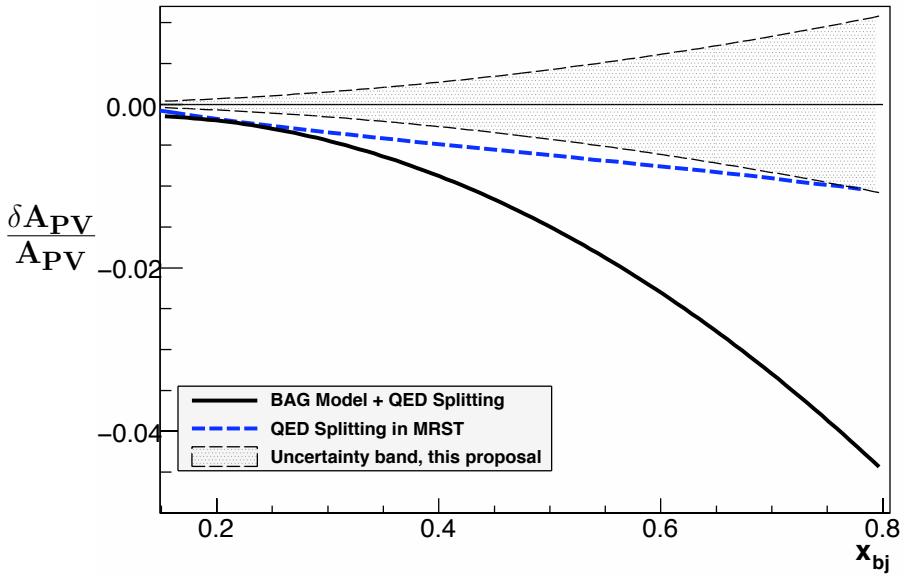

Figure 2.5: CSV predictions as a function of x. The vertical axis is the fractional change in A_{PV} due to CSV. The uncertainty band is the result of the fit discussed in Section 2.4.2. The MRST results shown here account for QED splitting in the Q^2 evolution only, and do not include non-perturbative QCD effects [19].

The corrections due to CSV for A_{PV} for deuterium are

$$\frac{\delta^{CSV} a_1^D}{a_1^d} = \left(\frac{3}{10} + \frac{2C_{1u} + C_{1d}}{2(2C_{1u} - C_{1d}}\right) R^{CSV}$$

$$\frac{\delta^{CSV} a_3^D}{a_3^d} = \left(\frac{3}{10} + \frac{2C_{2u} + C_{2d}}{2(2C_{2u} - C_{2d})}\right) R^{CSV}$$

The effect of the CSV suggested in Ref. [17, 18, 19, 20] on A_{PV} is plotted in Figure 2.5. The size of the CSV effect is within reach of our sensitivity.

Since we can obtain high precision in several narrow bins of x for $x > 0.4$ with the JLab upgrade, we will be in an ideal position to study CSV. In contrast to physics beyond the Standard Model, the effect depends strongly on x. This signature will be a powerful method for discriminating CSV from new physics as an explanation for any deviation from the prediction of Equation 2.4.

Although the Paschos-Wolfenstein ratio is more sensitive to R^{CSV}, neutrino experiments to date have not been able to obtain high statistics on small bins in the relevant kinematic range. Another approach to studying CSV is to measure asymmetries in W-production at colliders, but the experimental sensitivity is not very good [21]. Other possible CSV experiments include pion-induced Drell-Yan scattering and pion electroproduction sum rules [22, 23], but these approaches have complications such as fragmentation functions and CSV in sea quarks.

2.3.2 Hadron Dynamics Beyond Leading Twist

In terms of the complete description in terms of QCD, A_{PV} depends on five different structure functions as described in Appendix B.2. These structure functions have the effects of DGLAP evolution as well as power corrections, which are also called higher twist terms. The result is that Y_1 and Y_3 in Equation B.4 become functions of x, y, and Q^2, and a_1 and a_3 become functions of both x and Q^2.

It is convenient to discuss the corrections to the $Y_1 a_1$ and $Y_3 a_3$ terms separately. As shown in Section 2.3.2, the hadronic corrections to the small $Y_3 a_3$ term can be made empirically by using data on charged current neutrino scattering. The data have sufficient precision so that no other assumptions are required. The dominant $Y_1 a_1$ term is more interesting. As shown in the next section, the fact that the vector part of the current is conserved (CVC) implies that the only possible hadronic correction to the $Y_1 a_3$ term involves a correlation between up and down valance quarks. This correlation would be the only possible source of additional Q^2-dependence in the asymmetry. Such an effect, if present at a significant level, would be very interesting in itself.

CVC and the Interpretation of Higher Twist in the $Y_1 a_1$ Term

The term $Y_1 a_1^D$ involves only conserved vector currents. As a consequence, we can make a strong statement about possible hadronic corrections that were addressed by Bjorken [24], Wolfenstein [25], and Derman [26] shortly after the data of Prescott, et al. were published. Going back to the hadronic tensor in terms of currents, we can write a_i^D as

$$Y_1 a_1^D \propto \frac{L_\gamma^{\mu\nu} \sum_X \{\langle X|J_\mu^{ZV}|\rangle^* \langle X|J_\nu^\gamma|D\rangle + H.C.\}(2\pi)^3 \delta(P_X - p - q)}{L_\gamma^{\mu\nu} \sum_X \{\langle X|J_\mu^{\gamma}|\rangle^* \langle X|J_\nu^\gamma|D\rangle + H.C.\}(2\pi)^3 \delta(P_X - p - q)}$$

where J^{ZV} is the vector part of the weak current. Next, we decompose the vector currents in terms of isospin

$$V_\mu = (\overline{u}\gamma_\mu u - \overline{d}\gamma_\mu d); \quad S_\mu = (\overline{u}\gamma_\mu u + \overline{d}\gamma_\mu d)$$

and define

$$\langle VV\rangle = L_\gamma^{\mu\nu} \sum_X \langle X|V_\mu|D\rangle^* \langle X|V_\nu|D\rangle (2\pi)^3 \delta(P_X - p - q)$$

with similar expressions for $\langle SS\rangle$ and $\langle SV\rangle$

Then the asymmetry is proportional to

$$Y_1 a_1^D \propto \frac{(C_{1u} - C_{1d})\langle VV\rangle + \frac{1}{3}(C_{1u} + C_{1d})\langle SS\rangle}{\langle VV\rangle + \frac{1}{3}\langle SS\rangle} \tag{2.8}$$

The key here is that the $\langle SV\rangle$ term vanishes in the absence of CSV. (Strange quarks, which violate CVC, are accounted for explicitly in Equation 2.4. Their contribution is small.)

have also been neglected. If $\langle VV\rangle = \langle SS\rangle$, the hadronic structure completely cancels. The difference between $\langle VV\rangle$ and $\langle SS\rangle$ can be written

$$\langle VV\rangle - \langle SS\rangle = \langle (V - S)(V + S)\rangle \propto$$

$$L_\gamma^{\mu\nu} \sum_X \{\langle X|\overline{u}\gamma_\mu u|D\rangle^* \langle X|\overline{d}\gamma_\nu d|D\rangle + H.C.\}(2\pi)^3\delta(P_X - p - q) \tag{2.9}$$

If this expression vanishes, all of the hadronic structure in Equation 2.8 cancels and the $Y_1 a_1^D$ part of the asymmetry is strictly independent of Q^2. The right hand side of Equation 2.9 is a correlation between u and d quarks. Thus any Q^2 dependence observed in this term will be a measure of quark correlations. The only assumption is that the hadronic vector current is conserved (CVC).

The valence PDFs drop rapidly after $x \sim 0.3$. However, the x relevant to the quark-quark correlation function is the sum of the individual x-values of each quark, so it is likely that the correlation function doesn't fall rapidly until $x \sim 0.6$ or so. Thus the ratio of diquarks to single quarks may be strongly enhanced at large x. This argument suggests that the x-dependence of the diquarks could be similar to the observed x-dependence of the higher twist coefficients $C(x)$. Thus the observation of Q^2-dependent effects in PVDIS would be of particular interest [27].

Based on the above ideas, one method to remove the contribution of higher twist terms is to do a global fit of the form $D(X) = \alpha(1-x)^{-n}$, where α and n are parameters to be fit. If little Q^2-dependence is observed, tight bounds on the amplitudes will be found for $n > 2$. In this scenario, the contribution of the uncertainties in the higher twist coefficient to the high Q^2 point at $x \sim 0.4$ would be small.

Theories of Higher Twist

There are many descriptions available to discuss the physics of higher twist in QCD. Here we will use the operator product expansion as described for DIS by Jaffe and Soldate [28, 29]. First, a few comments on nomenclature. DIS is called leading twist, or twist-2. The spin structure function g_2 has a twist-3 contribution. The first correction to most of the other structure functions is twist-4. There is a list of all possible twist-4 operators in Appendix A of Ref. [29]. The first six are quark-quark term, and the remaining terms are quark gluon. Figure 2.6 gives the quark-quark correlation observable in PVDIS as well as an example of a quark-gluon diagram, the latter of which drops out in the $Y_1 a_1$ ratio. The ability to isolate quark-quark effects from quark-gluon terms is a special feature of PVDIS. Presently, no higher-twist data directly validates the existence of the interesting quark-quark terms.

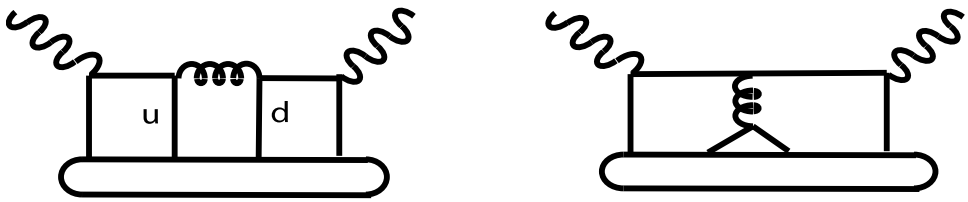

Figure 2.6: Left: Diagram of a quark-quark higher twist term. Right: Diagram of a quark-gluon correlation. The two quarks connected to the gluon in the middle can be eliminated by the QCD equations of motion

Calculations for higher twist in PVDIS have been done in the bag model by [30] and Secco [31]. The predictions are that the contribution of higher twist for our kinematics is negligible. However, the only quark-quark correlations in the bag model are those that must arise because the quarks are localized to a finite region the size of the nucleon. Thus, any effects that PVDIS might detect would be due to additional dynamics.

Data on Higher Twist

From the extensive data on structure functions, there is significant information on the presence of higher twist terms. These terms have proven to be rather small, but finally have been revealed by the precise data. There is interest in higher twist both as a function of x as well in the Q^2-dependence in the moments of the structure functions, which are more directly calculable in terms of QCD than the x-dependence itself. The most specific higher twist measurement involves g_2 after the twist-2 part is subtracted, and its first moment, d_2 [32, 33]. Only quark-gluon diagrams can contribute in this case. Other measurements presumably involve both quark-quark and quark-gluon contributions. A study of higher twist in the moments of g_1 at low Q^2, which has significant contributions form resonances, has shown evidence for large twist-6 and twist-8 contributions but small twist-4 contributions [34, 35]. On the other hand, studies of the behavior of higher twist in structure functions for kinematics above the resonance region are consistent with the presence of only twist-4 contributions [36].

A remarkable feature of DIS behavior is that higher twist effects for data where the mass of the final state $W > 2$ GeV are found to be small. For example, the higher twist terms have been determined recently for the measured e-p DIS structure functions $F_2(x, Q^2)$ [16] after the DGLAP evolution is removed. The ansatz is

$$F_2^\gamma(x, Q^2) = F_2^\gamma(x)(1 + D(x)/Q^2)$$

It turns out that the values of the $D(x)$ depend upon how many orders of α_s are taken in the DGLAP evolution of the PDFs. At leading order (LO), the higher twist contributions are significant and similar to the results of older analysis [37, 38]. However, as higher orders are taken, NLO, NNLO, and NNNLO, $D(x)$ becomes quite small, especially for $x < 0.4$. The values of D_i for both LO and NNNLO are summarized in Table 2.1. Recently the work on higher twists has been extended to one more order [39].

To interpret the size of higher twist terms at large values of x, one must take into account the relationship between W, Q^2 and x:

$$Q^2 = (W^2 - M^2)/(1/x - 1).$$

If $W = 2$ GeV is taken as the threshold for DIS behavior, then there is a threshold Q^2 denoted Q_t^2. Values for Q_t^2 are also given in Table 2.1. The maximum size of the higher twist effect that can be measured is thus $D(x)/Q_t^2$, which is also given in Table 2.1 as a fraction of $F_2^\gamma(x)$. This fraction is large enough to motivate a measurement only at high x.

Table 2.1: Higher twist coefficients $D(x)$ from Ref. [16].

x	$D(x)$ (LO)	$D(x)$ (N^{3}LO)	Q_t^2	$D(x)/Q_t^2$ (%) (LO)	$D(x)/Q_t^2$ (%) (N^{3}LO)
0.15	-0.07	0.01	0.5	-14	0.2
0.25	-0.11	0.00	1.0	-11	0
0.35	-0.06	-0.01	1.7	-3.5	-0.059
0.45	0.22	.11	2.6	8	4
0.55	0.85	0.39	3.8	22	10
0.65	2.6	1.4	5.8	45	24
0.75	7.3	4.4	9.4	78	47

We can include higher twist terms in $a_1(x)$ by defining

$$a_1(x, Q^2) = a_1(x)(1 + C(x)/Q^2).$$

As described in the next section, it is only quark-quark correlation that contributes to $C(x)$, whereas many possible higher-twist operators might contribute to $D(x)$. Hence it is plausible that $C(x) \leq D(x)$. Based on this assumption and Table 2.1, higher twist effects in $C(x)$ are probably impractical to isolate in PV DIS for $x < 0.4$. However, for $0.5 < x < 0.7$, it is possible that these effects could be observed cleanly. Moreover, since the effects of the DGLAP evolution cancel in the ratio $a_1^D(x)$, there is no problem with the order to which the evolution is performed.

The $Y_3 a_3$ Term

The $Y_3 a_3$ term is proportional to a ratio of neutrino scattering cross sections.

$$Y_3(x, y, Q^2) a_3(x, Q^2) \propto \frac{\sigma^{\nu D} - \sigma^{\bar{\nu} D}}{\sigma^{\nu D} + \sigma^{\bar{\nu} D}}$$

where $\sigma^{\nu D}$ is the cross section as a function of x, y, and Q^2 for charge current neutrino scattering and $\sigma^{\bar{\nu} D}$ is for anti-neutrino scattering. Here a small, calculable correction for the mass of the muon is neglected. The proportionality constant involves only electroweak couplings.

There is extensive data on neutrino scattering from approximately isoscalar targets that have sufficient precision for our purposes. Since we are taking a ratio, some experimental errors cancel and also there is cancellation of target mass corrections. The global analysis of Ref [36] shows that the higher twist terms are already constrained to be unimportant for out experiment, and new data from the MINERVA [40] experiment at Fermilab should improve out knowledge.

2.3.3 Summary of Higher Twist

In summary, the study of higher twist in PVDIS is of interest for the following reasons:

1. There are widely different estimates from among dynamical models about the size, both relative and absolute, of the various twist-4 matrix elements.

2. Parity-conserving DIS cannot distinguish between quark-quark and quark-gluon higher twist. For charged lepton scattering. there are two structure functions F_2 and F_L that involve three independent operators. Neutrino scattering is sensitive to F_3, which involves another independent quark-gluon operator.

3. The quark-quark operators are the only twist-4 operators that might be computed on the lattice in the foreseeable future.

The ability to isolate a quark-quark operator is thus of significant interest.

2.4 Data Strategy for a Deuterium Target

2.4.1 Kinematic Points

We plan to run for 120 days at 11 GeV and 60 days at 6.6 GeV. We assume a beam current of 50 μA and a polarization of 85%. The projected error bars for a selected binning over x and Q^2 is shown in Figure 2.7. All points have $W^2 > 4$ GeV^2. Most bins have $Y_3 \sim 0.84$. For $0.3 < x < 0.6$, there is a dynamic range of a factor of two in Q^2. There is one bin with average $x \sim 0.7$.

2.4.2 Fit of Asymmetry Data

The observation of CSV is possible with our apparatus only if the effect varies with x. An x-independent CSV effect would be indistinguishable from a change in the C_{1q}'s. It is quite natural, however, to expect that the x-dependence is similar to that shown in Figure 2.5, and we will make that assumption in our further discussion. From observations of higher-twist contributions to DIS cross sections, it is also natural to assume that Q^2-dependent effects will also increase with increasing x.

Under these assumptions, independent sensitivity to the various possible contributions depends critically on the ranges of x and Q^2 which can be explored with precision measurements of A_{PV}^D. With the projected data displayed in Figure 2.7, we can obtain asymmetries at the same x and y with a dynamic range in Q^2 of about $\sqrt{2}$. The dynamic range is obtained by comparing the 11 GeV data with the 6.6 GeV data. We can improve this dynamic range in Q^2 to a factor of 2 by allowing the value of y to change slightly, by about $\Delta y \sim 0.2$. The uncertainty introduced, which is due only to uncertainty in the C_2's times Δy, is negligible. This applies for values of x up to 0.6.

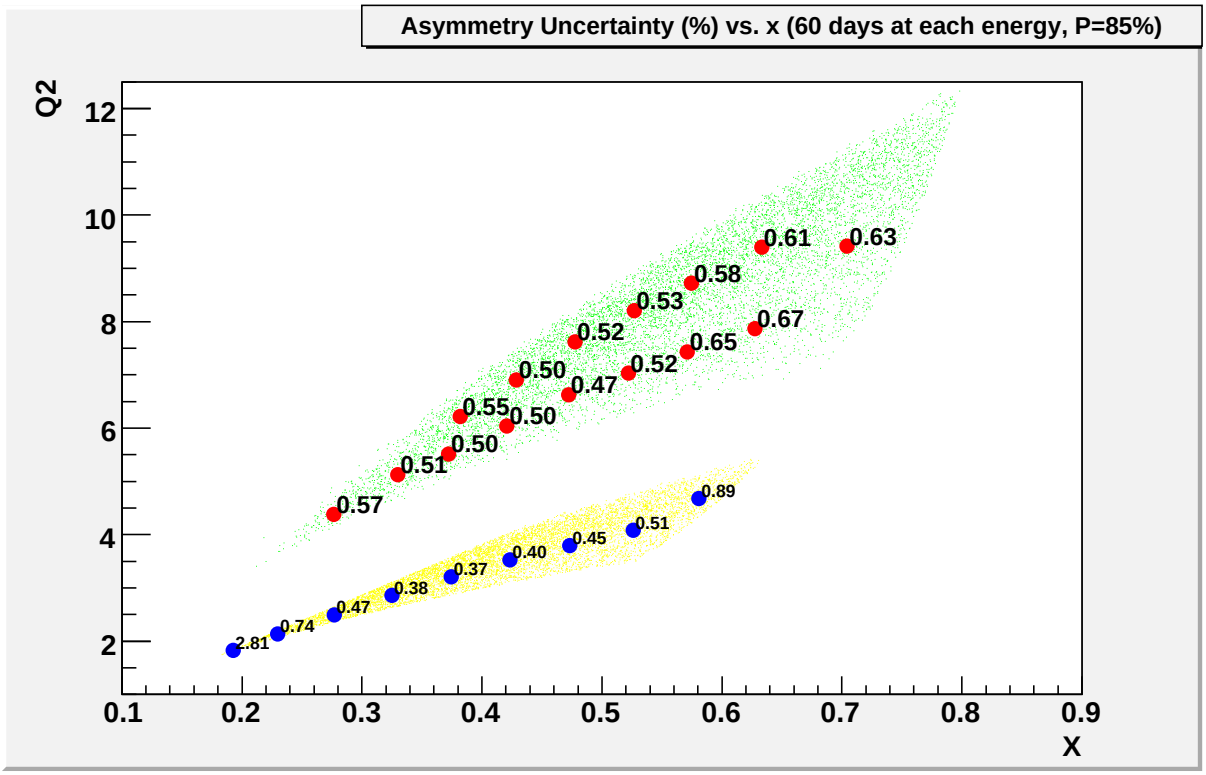

Figure 2.7: Errors in percent for A_{PV} for bins in Q^2 and x. The running times are 120 days with an 11 GeV beam and 60 days with a 6.6 GeV beam. The beam current is 50μA with a polarization of 85%.

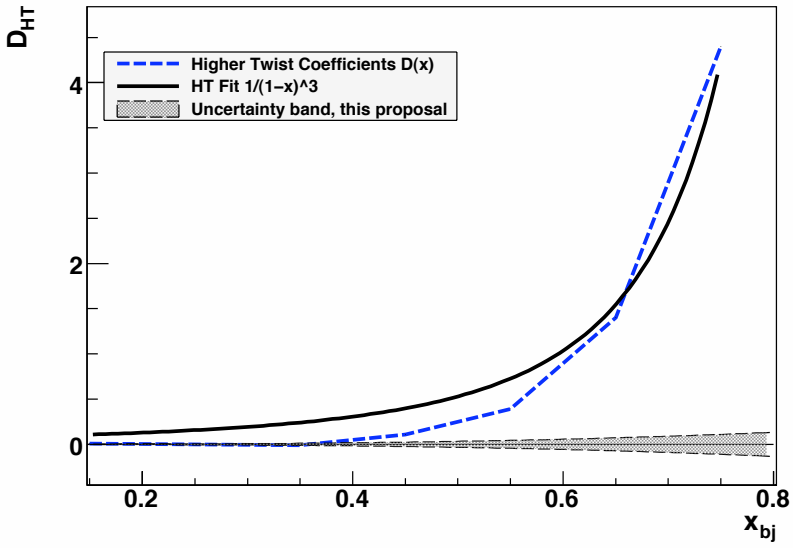

Figure 2.8: Demonstration of sensitivity to Q^2-dependent effects. Plotted are the higher-twist coefficients $D(x)$ from Ref. [16], listed in Table 2.1. Also shown is a fit to these coefficients using the form $(1-x)^{-3}$. The uncertainty band is the result of the fit discussed in Section 2.4.2.

To untangle the effects of hadronic and electroweak physics, we plan to fit the asymmetries to a function of the form

$$A_{PV}^{D} = A_{PV}^{EW}\left(1 + \beta_{HT}\frac{1}{(1-x)^3 Q^2} + \beta_{CSV}x^2\right) \tag{2.10}$$

The resulting statistical errors on the fit parameters are:

$$\delta A_{PV}^{EW}/A_{PV}^{EW} = 0.3\%; \quad \delta\beta_{HT} = 0.0026; \quad \delta\beta_{CSV} = 0.017$$

With this method, we use the full statistical power of the data set. However, the result has some sensitivity to the exact form of the chosen fitting functions. Under the scenario where the hadronic effects are small, these errors are negligible as long as we assume that CSV and higher twist effects depend strongly on x, as expected. The one-sigma band for the CSV term is plotted in Figure 2.5, the corresponding band for the higher-twist term is shown in Figure 2.8.

If the pattern of higher twist effects is the same for A_{PV} as it is for the cross sections (Sec. 2.3.2, Table 2.1), then at $x = 0.6$ the asymmetries at the different Q^2 values will differ by 15%. In that scenario, the rapid x-dependence of the higher-twist coefficients for the cross section would imply that higher twist effects would still be negligible at $x = 0.4$. This scenario is illustrated in Fig. 2.8. With a comparable x-dependence, a Q^2-dependent effect as small as $\sim$1/30th of the effect seen in cross-section measurements would be easily identifiable given our statistical precision.

Table 2.2: Error budget in A_{PV}^{EW} at $x = 0.4$ for the test of the Standard Model

Source	Uncertainty in %
Statistics	0.3
Polarimetry	0.4
Q^2	0.2
Radiative Corrections	0.3
Total	0.6

2.4.3 Sensitivity to Physics Beyond the Standard Model

If the hadronic terms are omitted from the fit, the error in A_{PV}^{EW} is 0.1%. The 0.3% error we quote from the fit is effectively dominated by an extrapolation error. The error on A_{PV}^{EW} increases to 0.6% when the systematic errors listed in Table 2.2 are included. This error corresponds to the vertical axis on Figure 2.4.

Presently, the atomic parity-violation in Cs is the most sensitive measurement of a combination of the C_{ij}'s, the parity-violating couplings in electron-quark sector. After the data on PVDIS and Qweak are obtained, there will be two more measurements of similar precision. One might then ask which of the experiments is most sensitive to new physics. Strictly speaking, there is no model-independent answer to this question. However, it is reasonable to assume that deviations δC_{ij} in any of the couplings are equally likely. In that spirit, the regions allowed by the measurements should be plotted on scales with equal units for each of the C_{ij} as we have chosen to do in Figures 2.2 and 2.3.

Equivalently, one can express the result of any measurement as a normalized linear function $M(C_{ij})$

$$M(C_{ij}) = \sum_{ij} \alpha_{ij} C_{ij}; \quad \sum_{ij} |\alpha_{ij}|^2 = 1$$

so that the experiments with the smallest value for δM are the most sensitive to new physics. Table 2.3 gives the projected results in this method. A final measure, which is more subjective, is the error in $\sin^2\theta_W$. A plot of the sensitivity of various experiments to $\sin^2\theta_W$ is given in Figure 2.1. PVDIS does well by this measure, with a sensitivity of $\delta \sin^2\theta_W = 0.0006$.

If a large violation of the Standard Model is observed, measurements made with the maximum possible difference in Y can be used to separate the contributions from the C_{1q}'s and the C_{2q}'s. By comparing data at 12° and 35°, a dynamic range in the difference of $\Delta Y \sim 0.5$ can be achieved. However, the Q^2 values will be ~ 3 GeV^2 for the lowest Y and ~ 6 GeV^2 for the highest Y. The procedure can be justified if the observed higher twist effects are negligible at large x and assumed to be much smaller at lower x.

Table 2.3: Comparisons of the different parity-violation experiments in the electron-quark sector by two different criteria

Experiment	$M(C_{ij})$	δM	$\delta \sin^2\theta_W$
APV (Cs)	$0.67C_{1u} + 0.75C_{1d}$	0.0007	0.0014
Qweak	$0.89C_{1u} + 0.45C_{1d}$	0.0007	0.0007
PVDIS	$0.68C_{1u} - 0.34C_{1d}$		
	$+0.58C_{2u} - 0.29C_{2d}$	0.0017	0.0006

2.4.4 Summary of the Deuterium Program

This experiment, like the strange quark experiments before, is almost guaranteed to provide answers to one or more significant questions: Are there large CSV effects in the parton distributions? Is there evidence for significant quark-quark correlations that lead to a departure from the parton model at moderate Q^2? If SUSY is seen at the LHC, do we have evidence for the breaking of R-parity which would (a) preclude conventional WIMP dark matter in the MSSM and (b) imply that neutrinos are Majorana particles?

2.5 Physics with Other Targets

2.5.1 Measuring d/u for the proton at high x

Another important issue in DIS is the ratio of down quarks to up quarks, $d(x)/u(x)$, in the proton. The traditional method for measuring this ration is to assume charge symmetry and use the deuteron as a neutron target. Unfortunately, nuclear corrections introduce a large uncertainty at large x [41, 42, 43, 44]. At JLab, a number of methods have been proposed to circumvent the problem. One is to compare ^{3}He with tritium. Another, developed by the BONUS collaboration [45], is to tag the recoil proton and thereby control the expected dominant corrections. However, PVDIS from hydrogen is sensitive to $d(x)/u(x)$ and completely avoids any nuclear corrections. In particular, the dominant term in the asymmetry is given by

$$a_1^p(x) = \left[\frac{12C_{1u}u(x) - 6C_{1d}d(x)}{4u(x) + d(x)}\right]$$

$$\sim \left[\frac{u(x) + 0.912d(x)}{u(x) + 0.25d(x)}\right]$$

Precision measurements in the range of x from 0.6 and 0.7 would be of great interest.

The fractional error in d/u is roughly twice the fractional error in A_{PV}. If the higher twist contribution to A_{PV} for the deuteron is negligible, we will also neglect higher twist

for the hydrogen data. We estimate that we can obtain a 2% error on d/u over a range of x bins, with the highest having an average $x = 0.7$, in 90 days of running. The achievable precision is illustrated in Figure 2.9.

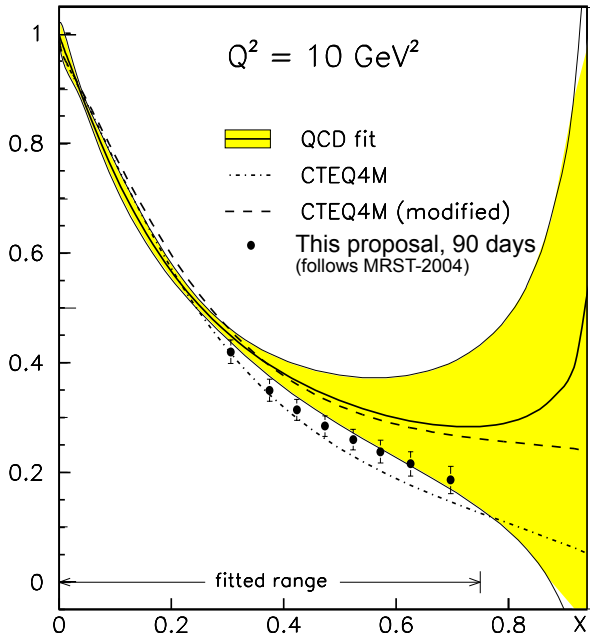

Figure 2.9: Uncertainties in d/u together with error bars corresponding to results from A_{PV} for a hydrogen target.

2.5.2 Induced Nuclear Isospin Violation

The ratio of the structure functions between complex nuclei and deuterium

$$R^{\gamma}_{EMC} = \frac{4u_A(x) + d_A(x)}{4u(x) + d(x)} \tag{2.11}$$

where $u(d)_A$ is the normalized PDF for quarks in the nucleus, have been observed to depend on x. For parity violation, the PDFs are weighted differently:

$$R^{\gamma Z}_{EMC} = \frac{1.16u_A(x) + d_A(x)}{1.16u(x) + d(x)} \tag{2.12}$$

The quantity that is practical to measure is the super-ratio

$$R_{Super} = \frac{A^A_{PV}}{A^D_{PV}} = \frac{R^{\gamma Z}_{EMC}}{R^{\gamma Z}_{EMC}} \tag{2.13}$$

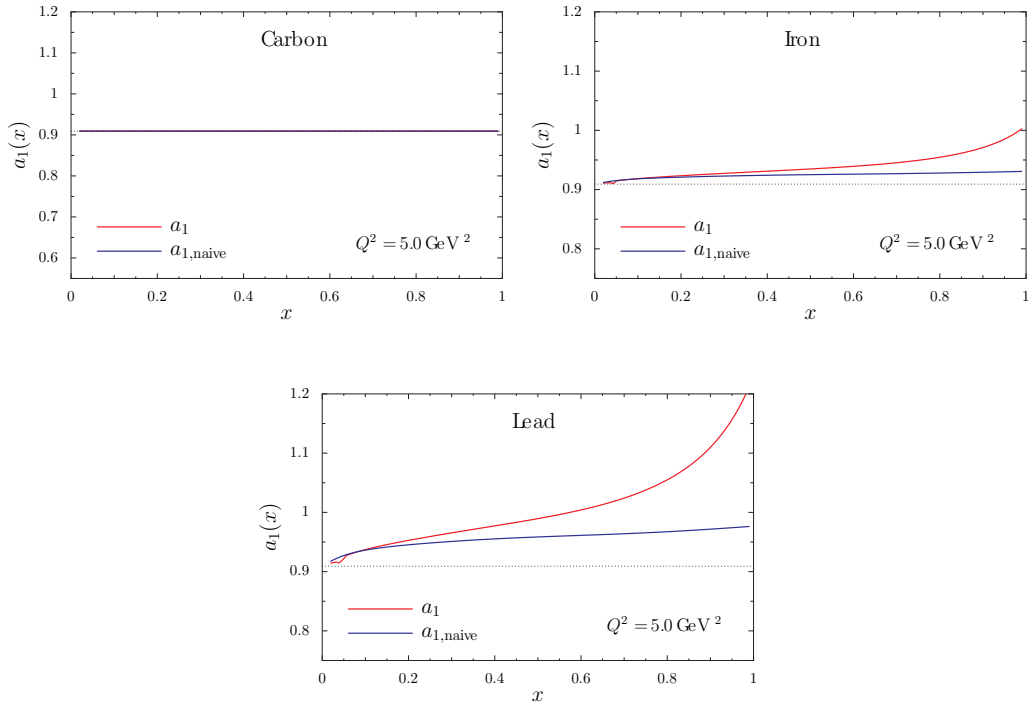

Figure 2.10: Theoretical predictions based on the NJL model described in the text for the super-ratio for various nuclei. For these calculations, there is no effect if $A = Z$.

Assuming CSV in the deuteron, any difference between the super-ratio and unity is sensitive to a violation of the equation

$$u_A = d_A \tag{2.14}$$

or simple extrapolations for the case where $N \neq Z$. In Figure 2.10, a theoretical prediction based in the presence of a vector potential in complex nuclei [46] is displayed that suggests that the effect in Pb is about 5% at large x, large enough to be observed in our experiment. The same effect can explain a large fraction of the NuTeV anomaly. The observation of a non-unity value for R_{Super} would be clear evidence that nucleon structure is fundamentally altered in the presence of nuclear matter. A measurement of this effect would be valuable and appears feasible in PVDIS. Although this proposal focuses on measurements with hydrogen and deuterium, this topic is mentioned as an example of further electroweak studies which would be enabled by the SoLID spectrometer.

Chapter 3

Apparatus

3.1 SoLID Engineering and Design

This section addresses a recommendation from PAC34 [47]:

"The feasibility of running other experiments by leaving the magnet itself in place and removing the target and detector packages must be examined in detail."

The ability to move the detectors and other equipment out of the yoke will be also necessary for servicing these elements, and will become an essential part of the mechanical design of the apparatus.

The design of the SoLID spectrometer has now undergone a more rigorous mechanical analysis, both in terms of engineering design of the end cap and baffle support and in terms of the feasibility of removing the detector end cap so that other experiments could be interleaved with those using the SoLID spectrometer. This section contains the results of those engineering and design studies[1]. The studies were done for the downstream endcap only, but the results can be applied as well for the simpler upstream endcap.

In brief, we have learned that it is going to be feasible to design the apparatus such that the detectors and the lead baffles are straightforward to remove and thus leave the beamline inside the superconducting coil available to run other experiments. Mounting and dismounting of the target has not been yet addressed. Such operations are common at JLab in all 3 halls, and the experience gained will be used in the target design for SoLID.

The main features of the spectrometer are shown in Fig. 3.1 along with the basic dimensions in Fig. 3.2. The magnet is shown in a cut-away state and is mounted on fixed supports. The baffle assembly is mounted by a cantilevered support connected to the end cap. The baffle assembly and the endcap are constructed in halves to allow them to open away from the beam pipe as described below.

[1] These engineering studies were carried out at Argonne National Lab.

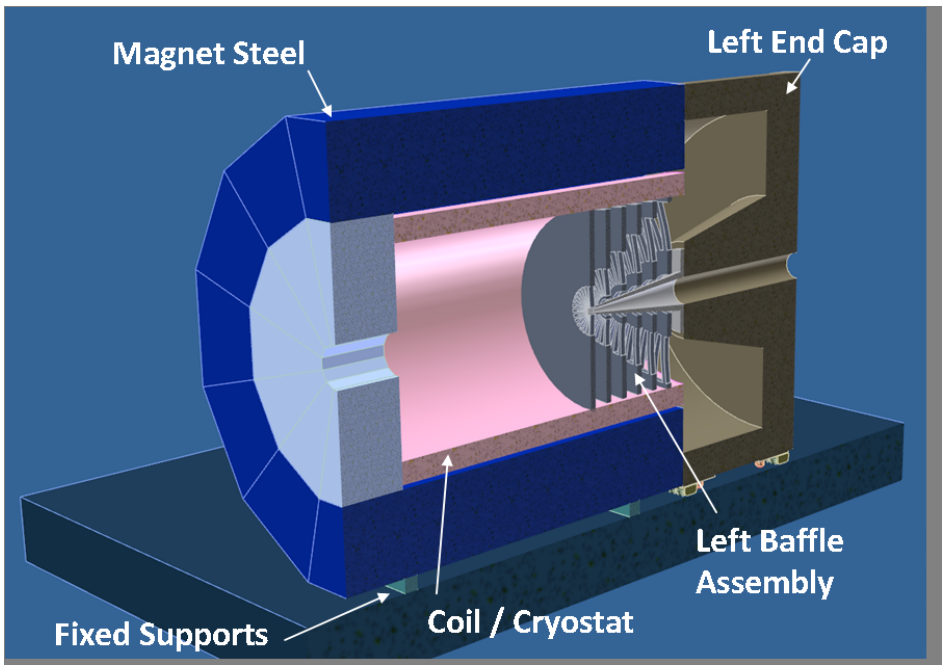

Figure 3.1: Cut-away view of the spectrometer and left end cap.

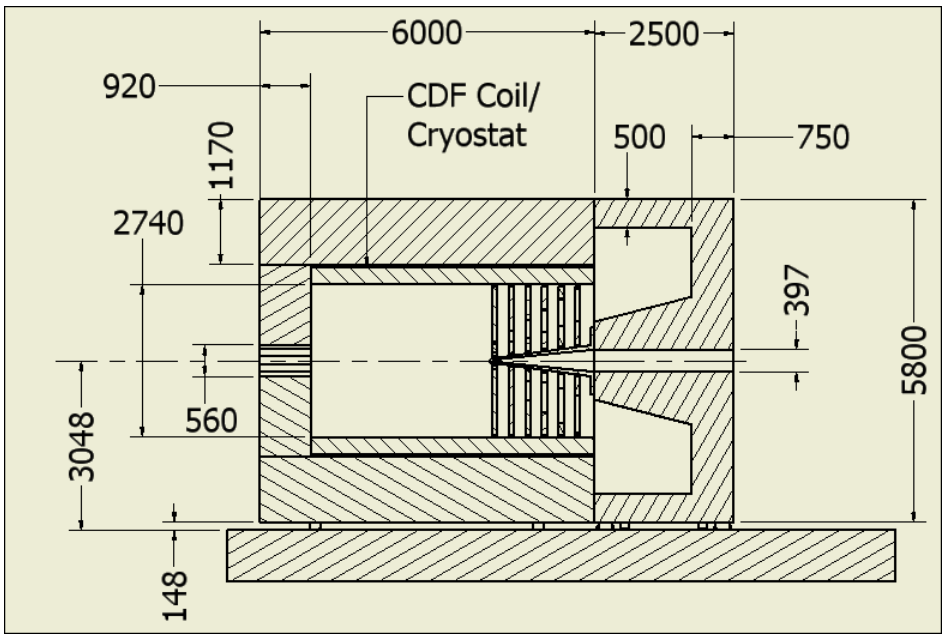

Figure 3.2: Basic dimensions of the spectrometer.

3.1.1 End Cap Movement Sequence

The design requires that the end cap be able to be moved out of the immediate experimental area. It is further required that this be accomplished without removing the beam pipe. To serve this purpose, the end cap is designed in two halves that can be separated. The spectrometer is shown in the closed position in Fig. 3.3. The first step in the opening sequence is to retract the end cap along the beam axis in order to bring the baffle assembly completely out from the interior of the magnet coil. The left and right end cap assemblies are supported by heavy duty rollers (discussed further below) and are rigidly connected together to move as a single body. The retract motion can easily be done by using hydraulic cylinders or cable winches. Figure 3.4 shows the relative position of the end cap at the extent of this motion.

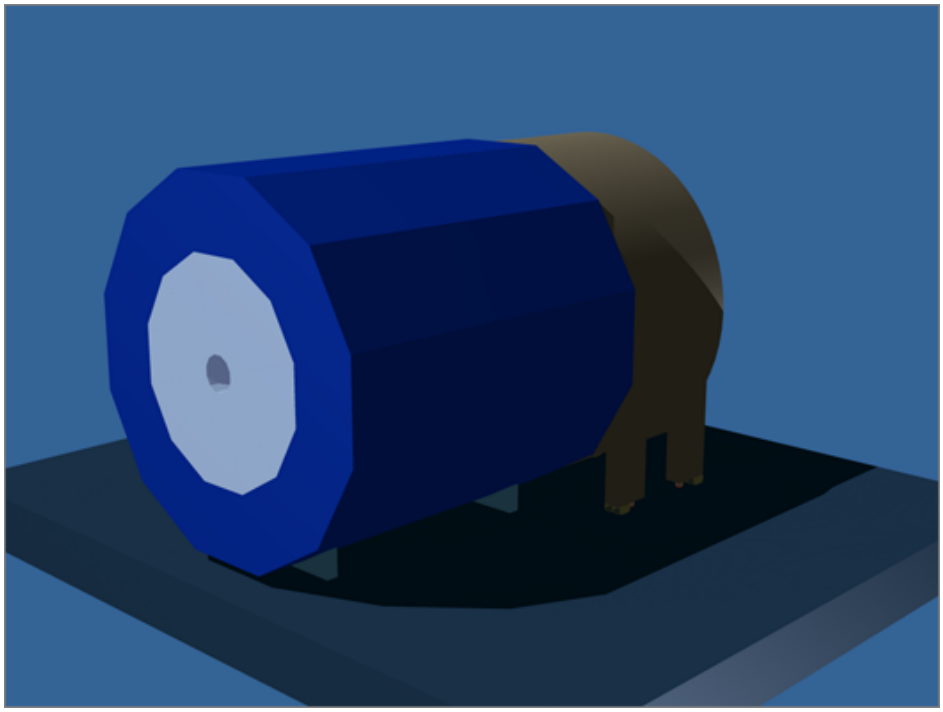

Figure 3.3: Spectrometer in closed position.

Figure 3.5 shows more detail of the roller support on the end cap. In the figure, the endcap is supported by the rollers and they are aligned in the direction parallel to the beam axis. Rollers are located at four points on each end cap. Next to each set of rollers is a hydraulic jack mounted upside down to the bottom of the end cap and initially in a retracted position such that they do not make contact with the ground. After the end cap is moved far enough along the beam line to clear the baffle assembly, the jacks are extended so that the rollers are raised off of the ground by a small distance. This action allows the rollers to be rotated 90 degrees to the opening orientation as shown in Fig. 3.6.

The final position of the opened end cap is shown in Fig. 3.7. As discussed below, the baffle assembly will require fixturing to support prior to being split in half.

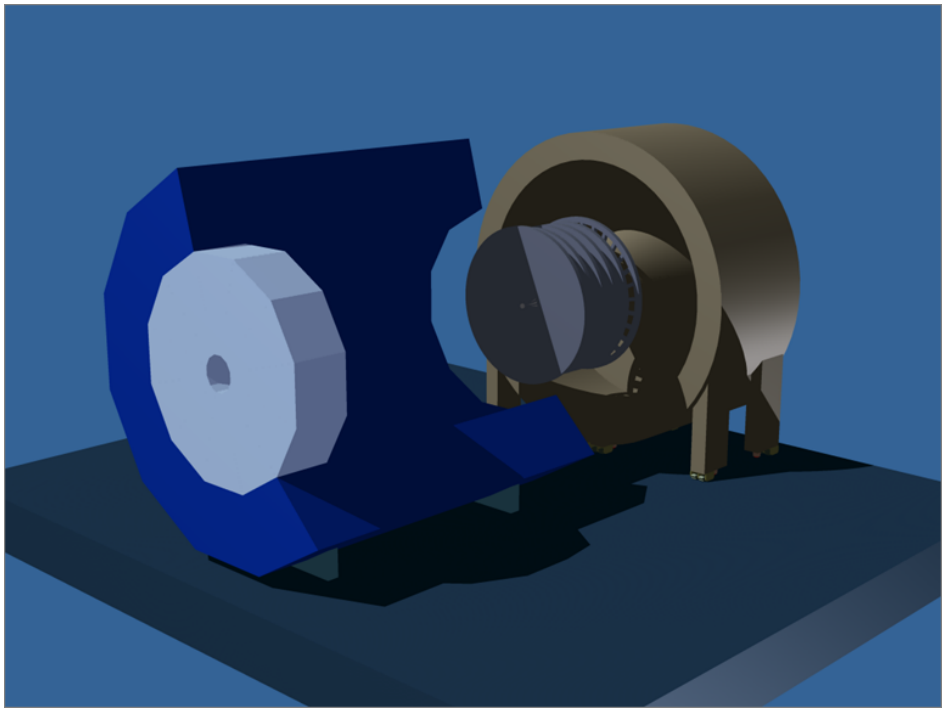

Figure 3.4: End cap and baffle assembly retracted along the beam axis. (Magnet cut-away and coil removed for clarity).

The endcap center of gravity lies nicely inside the support points for both the rollers and the jacks as shown in Fig. 3.8. Each individual end cap weight (along with $\frac{1}{2}$ baffle assembly) is approximately 172 metric tons. Without any lateral acceleration, the load is fairly evenly distributed between support points. The least stable situation is when the endcap is on jacks in the direction along the beamline. In this direction, it takes a 0.1 g acceleration through the center of gravity to tip the end cap. Note this is in the situation with the baffles removed which causes an unfavorable shift in the center of gravity as shown in Fig. 3.8.

The endcap is not exposed to lateral forces while on the jacks and the short time on the jacks should preclude the need to design to any seismic requirement which might be the only potential source of a lateral acceleration. It is difficult to imagine and accidental force capable of producing a 0.1g acceleration in the 172 metric ton end cap. During motion, the acceptable accelerations are much high (from a stability point of view) and it should be possible to limit the movement accelerations to much less than this value. Movement occurs at slow speeds and it can be shown that below certain speeds, there is not enough energy to tip the end cap even with dramatic sudden stops. Rollers and jacks capable of supporting 80 metric tons would provide sufficient safety factor against any increase support reactions due to any foreseeable lateral accelerations.

The use of rollers and hydraulics to support and move heavy objects is common both in industry and in high energy experiments. The CDF detector at Fermilab used Hilman rollers (such as those shown in Fig. 3.9) for opening the detector at access points.

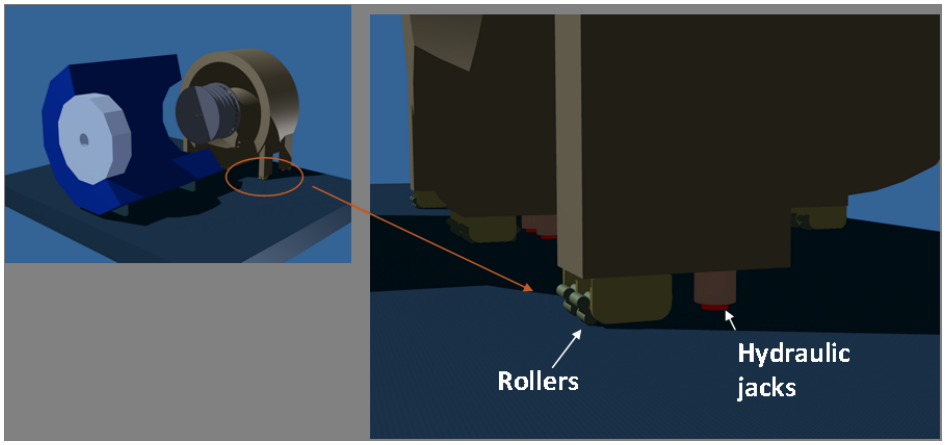

Figure 3.5: Endcap raised using hydraulic jacks allowing rollers to be rotated into the open/close orientation.

Figure 3.6: Endcap raised using hydraulic jacks allowing rollers to be rotated into the open/close orientation.

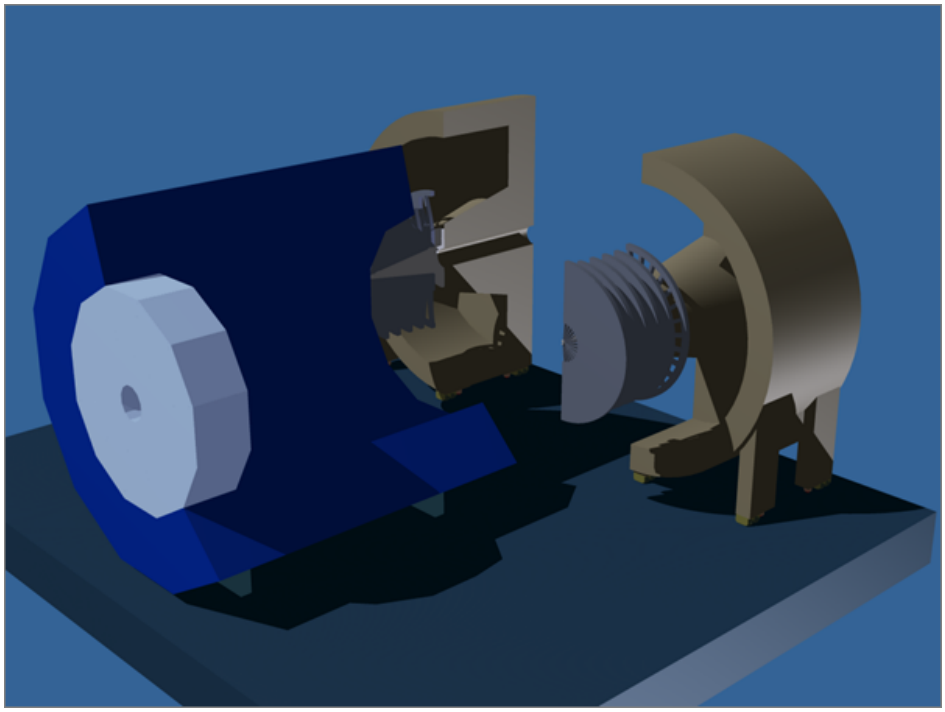

Figure 3.7: Endcap opened away from the beamline.

The ATLAS detector at CERN used hydraulic jacks (such as those shown in Fig. 3.10) mounted upside down and attached to the detector as proposed here for several large components in the detector. Jacks and rollers with capacity of 80 tons are commercially available within the limited height available for these components.

3.1.2 Baffle design

The lead baffle assembly is shown in Fig. 3.11. Each baffle assembly is approximately 14.5 metric tons. The baffles each have semi-circular holes on them and set on a stepped support shaft. Spacers (not shown in the figure) are used in combination with a lockring at the first baffle to locate the baffles against the stepped shaft. A key alignment feature will be created in each baffle to preserve the proper orientation while on the shaft. The baffles are mounted in this simple contact way to avoid making any structural connections through the lead or requiring that steel inserts be cast in place. They are not structurally stable in this configuration. Instead, the right baffle assembly (a mirror image of the left) is mounted simultaneously and a steel outer skin is wrapped around the circumference. This steel skin is shown in Fig. 3.12. Each of the left and right baffle assemblies will have this skin in contact and then the skin will be bolted together when the two halves are joined to create supporting band. This band will keep the lead baffles from falling away from the stepped shaft and also provides support. The stepped baffle support shaft is made of aluminum. Preliminary stress analysis using finite element analysis is shown in Fig. 3.13. Stresses are the aluminum support shaft (≈2500psi away from stress

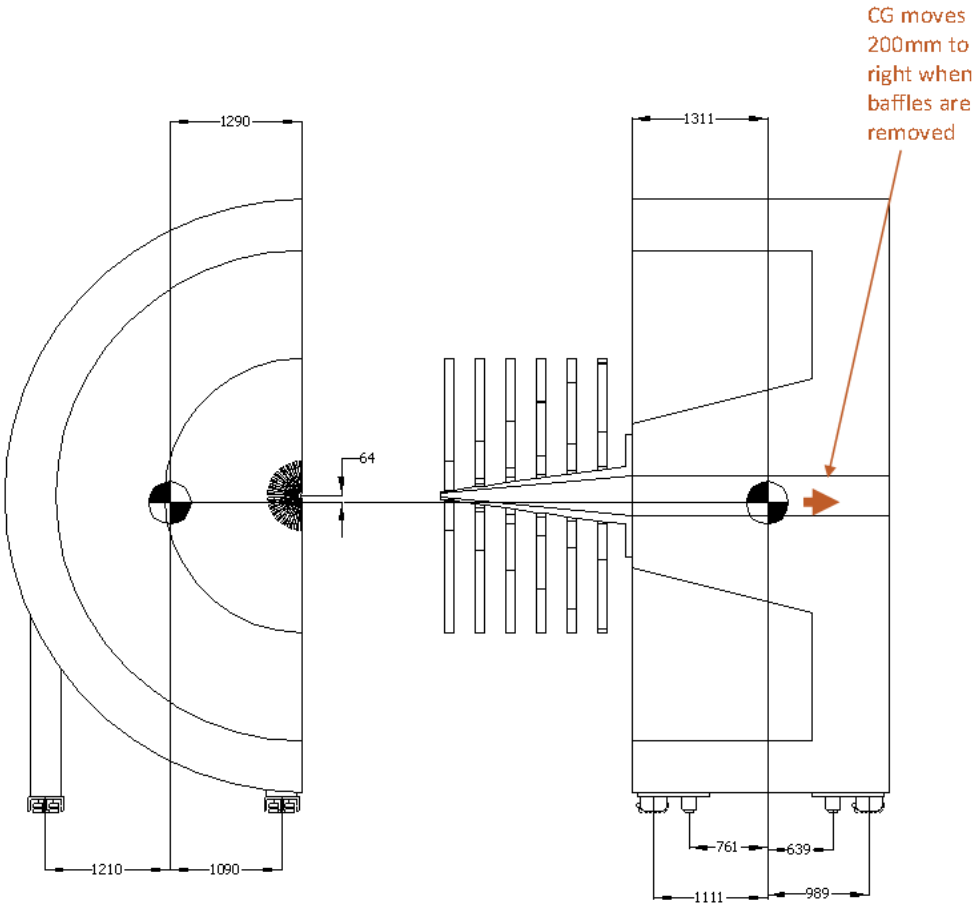

Figure 3.8: Left End cap center of gravity location relative to roller and jack support points.

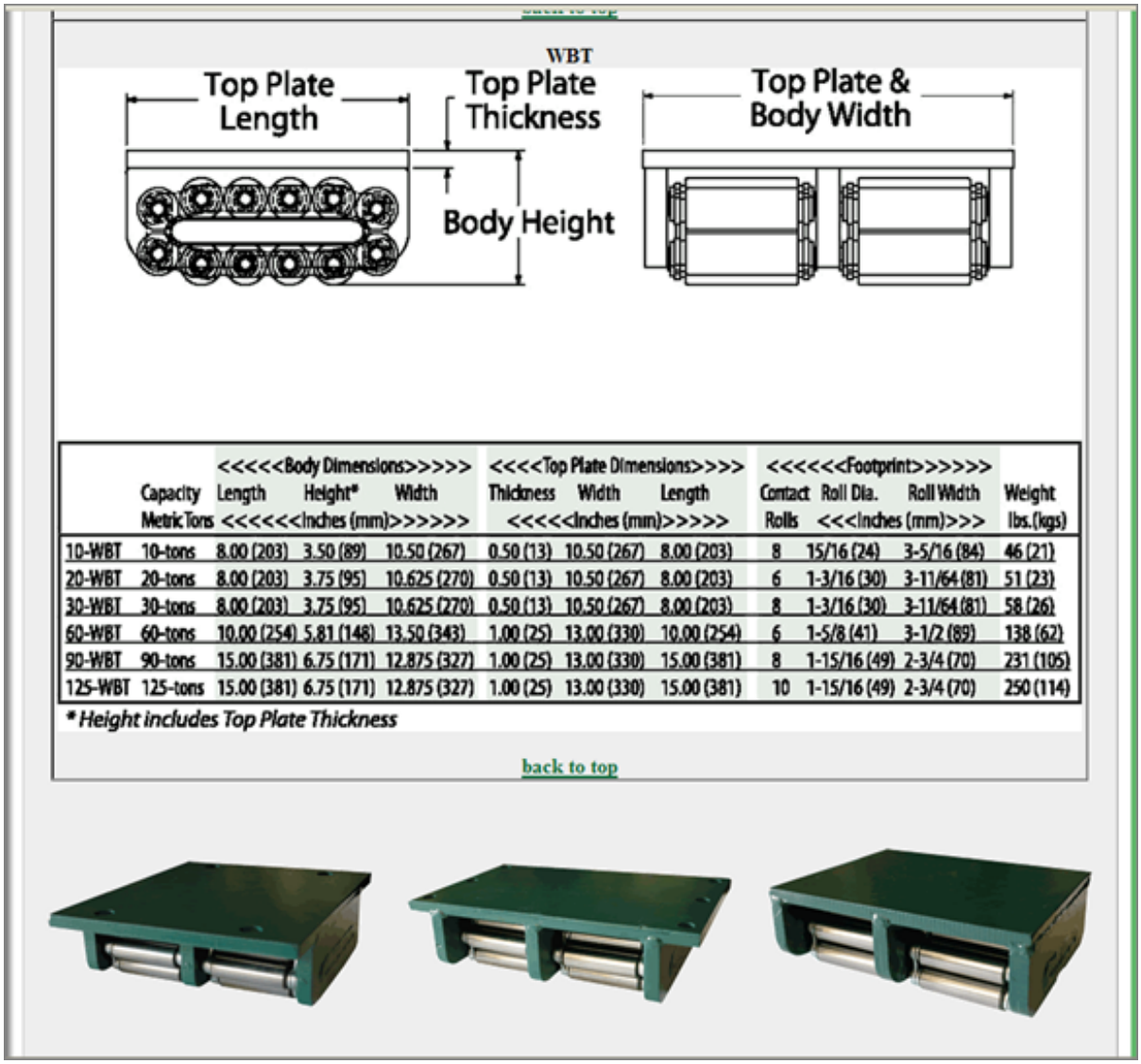

	Capacity	<<<<<Body Dimensions>>>>> Length	Height*	Width	<<<<Top Plate Dimensions>>>> Thickness	Width	Length	<<<<<<Footprint>>>>>> Contact Rolls	Roll Dia.	Roll Width	Weight
	Metric Tons	<<<<<<Inches (mm)>>>>>>			<<<<<Inches (mm)>>>>>				<<<Inches (mm)>>>		lbs.(kgs)
10-WBT	10-tons	8.00 (203)	3.50 (89)	10.50 (267)	0.50 (13)	10.50 (267)	8.00 (203)	8	15/16 (24)	3-5/16 (84)	46 (21)
20-WBT	20-tons	8.00 (203)	3.75 (95)	10.625 (270)	0.50 (13)	10.50 (267)	8.00 (203)	6	1-3/16 (30)	3-11/64 (81)	51 (23)
30-WBT	30-tons	8.00 (203)	3.75 (95)	10.625 (270)	0.50 (13)	10.50 (267)	8.00 (203)	8	1-3/16 (30)	3-11/64 (81)	58 (26)
60-WBT	60-tons	10.00 (254)	5.81 (148)	13.50 (343)	1.00 (25)	13.00 (330)	10.00 (254)	6	1-5/8 (41)	3-1/2 (89)	138 (62)
90-WBT	90-tons	15.00 (381)	6.75 (171)	12.875 (327)	1.00 (25)	13.00 (330)	15.00 (381)	8	1-15/16 (49)	2-3/4 (70)	231 (105)
125-WBT	125-tons	15.00 (381)	6.75 (171)	12.875 (327)	1.00 (25)	13.00 (330)	15.00 (381)	10	1-15/16 (49)	2-3/4 (70)	250 (114)

** Height includes Top Plate Thickness*

back to top

Figure 3.9: Spec. sheet from Hilman Rollers showing various standard available heavy duty roller sets.

Figure 3.10: Hydraulic blocking jacks.

concentrations) are well below allowable stressed for aluminum (≈18000psi for 6061-T6). Static buckling analysis (ignoring effects of creep) indicates a safety factor of 16 with respect to buckling. This value will be lower when creep effects are considered. This cannot be accurately determined without more precise material properties for lead but typically this value would not decrease by more than a factor of 3. The stresses in the lead ≈1000psi in some peak areas. Handbook values of typical CaSnPb Alloy indicates 1% creep strain in 8 years at 1000psi.

To first order this suggest there is no problem with this design. In the final design, more detailed creep analysis and checks on creep buckling will be needed once better material properties are understood. If creep is found to be greater than is acceptable, the baffle weight can be reduced in the outer radius of the first few baffles which would reduce the stress. A possible design is shown in Fig. 3.15. The stress analysis for this design is shown in Fig. 3.16. With the removal if the weight due to the lead in the outer radius, the stress in the lead is reduced to less than 250psi which will reduce the effects of creep. Additionally, buckling is greatly reduced in this case with a factor of ¿1000 against buckling in the linear case (again ignoring creep). This analysis shows a solution to exist. the optimal solution will be found after further design analysis.

The baffle geometry is shown in Fig. 3.17. To get a lead baffle with superior mechanical properties, common alloys of Ca-Sn-Pb are used. Mechanical properties of lead can vary greatly based on fabrication and particularly on rolling (see next comment) which improves mechanical properties. Preliminary discussions with lead vendors indicate that the geometry is within the size of available tooling to allow rolling after casting.

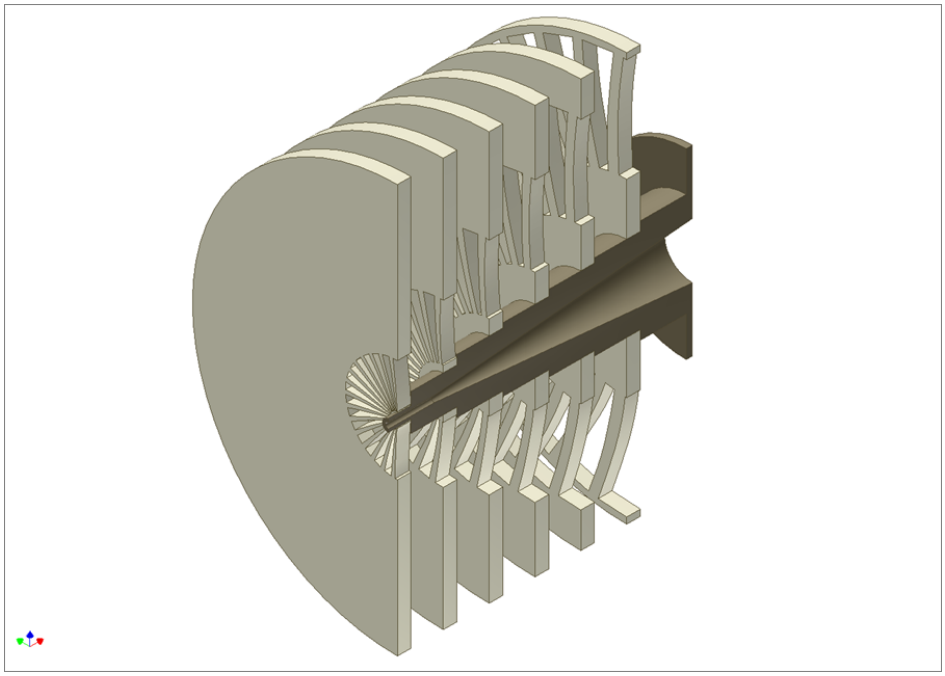

Figure 3.11: Left Baffle assembly.

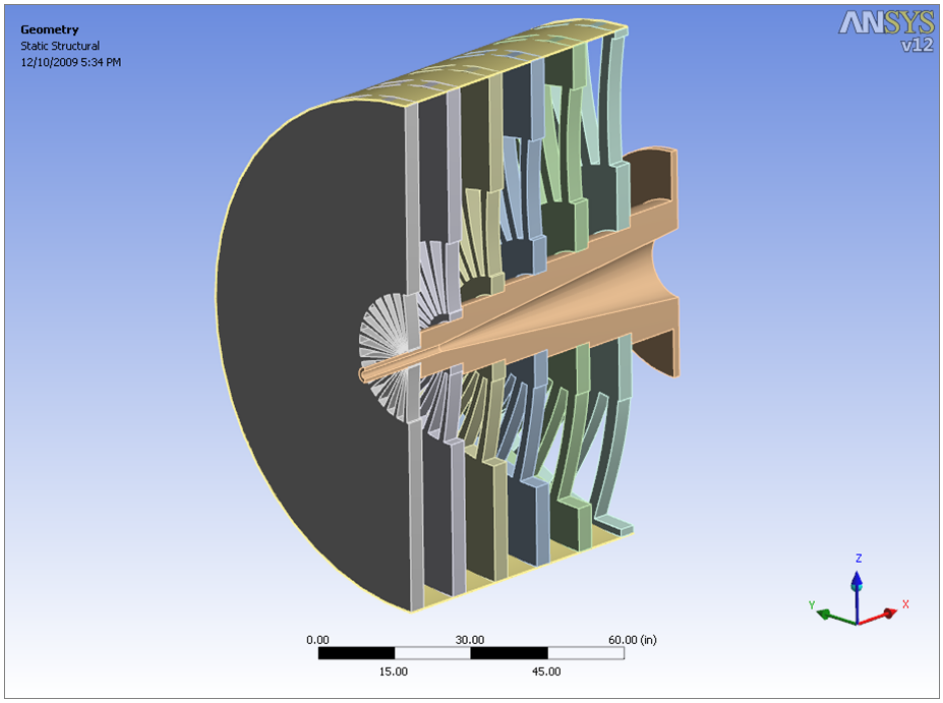

Figure 3.12: 1/2 symmetric analysis geometry showing a representation of the steel skin around the baffles.

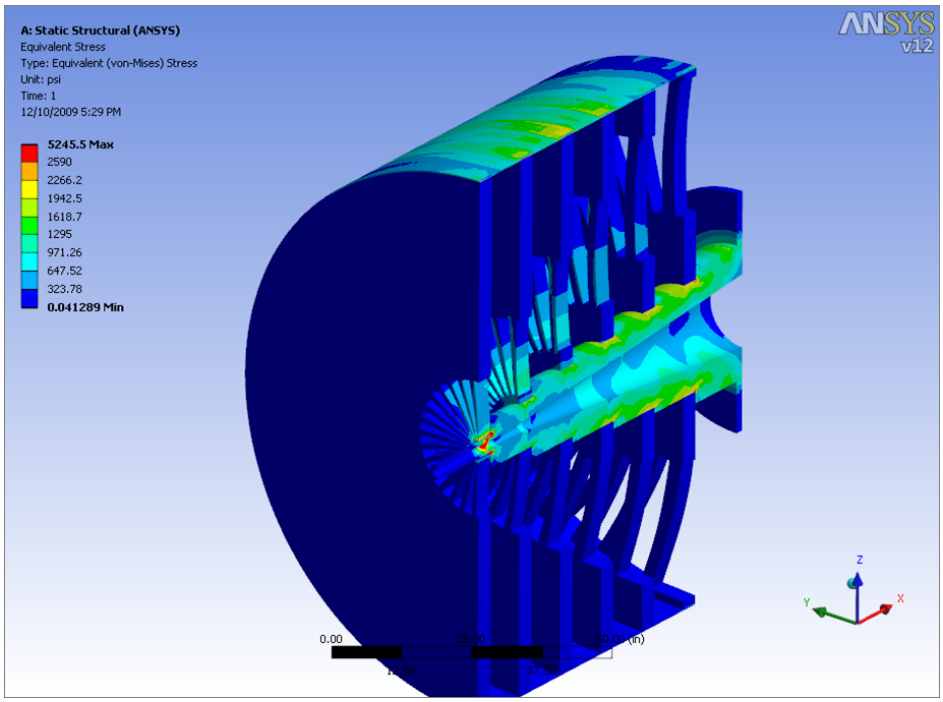

Figure 3.13: Von Mises stress of combined left and right baffle assemblies joined by circumferential metal banding. (1/2 symmetry model).

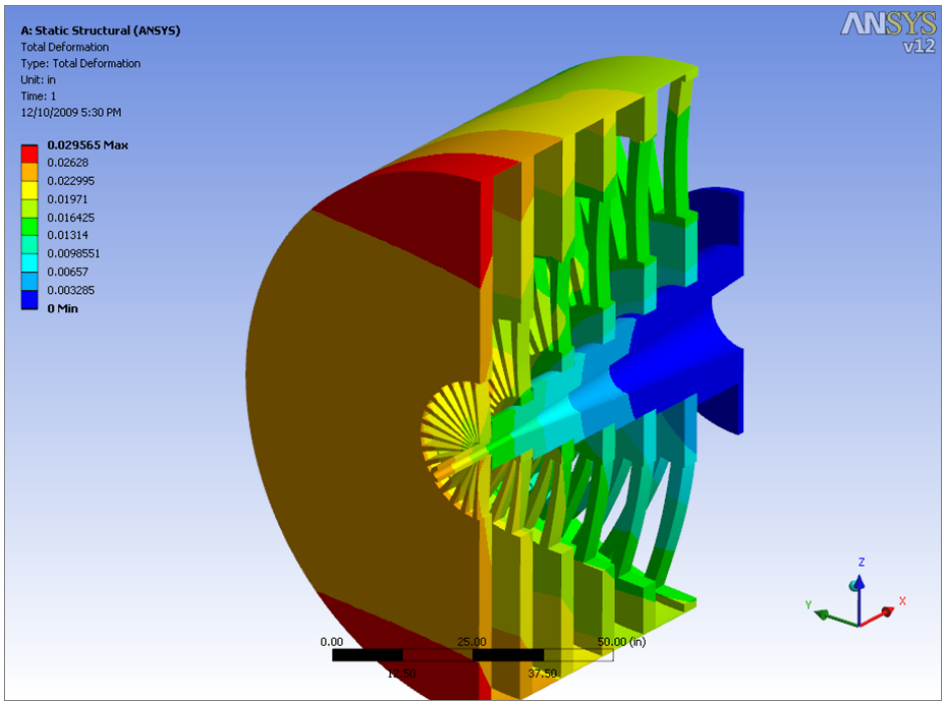

Figure 3.14: Resulting deflections of combined left and right baffle assemblies joined by circumferential metal banding. (1/2 symmetry model).

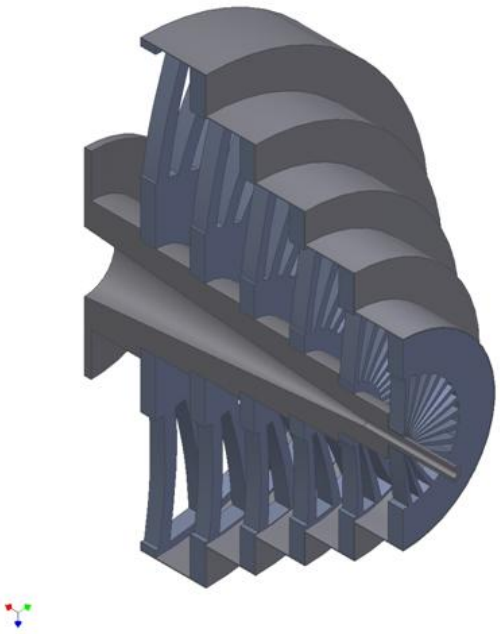

Figure 3.15: Stepped baffle design.

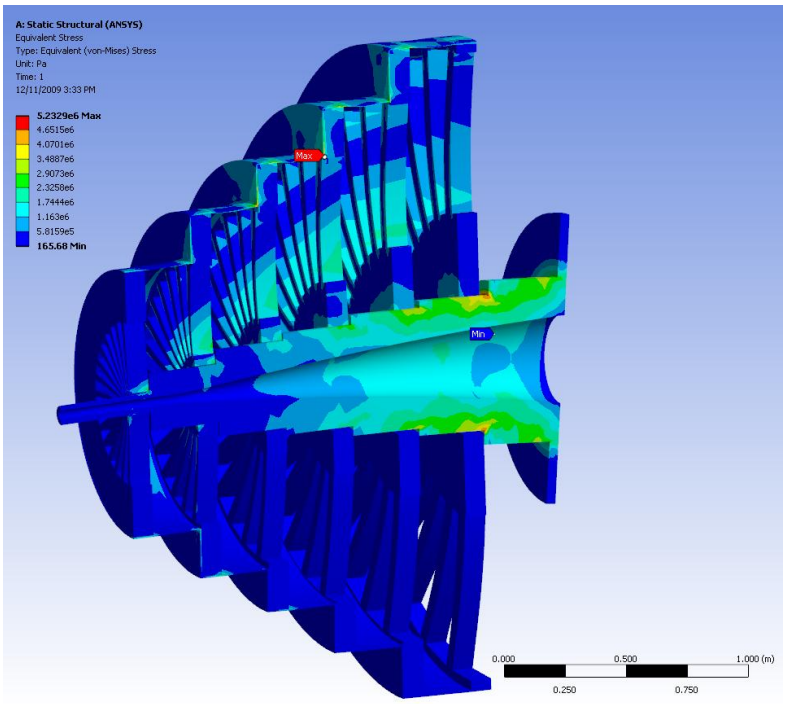

Figure 3.16: Von Mises Stress for alternate stepped baffle design.

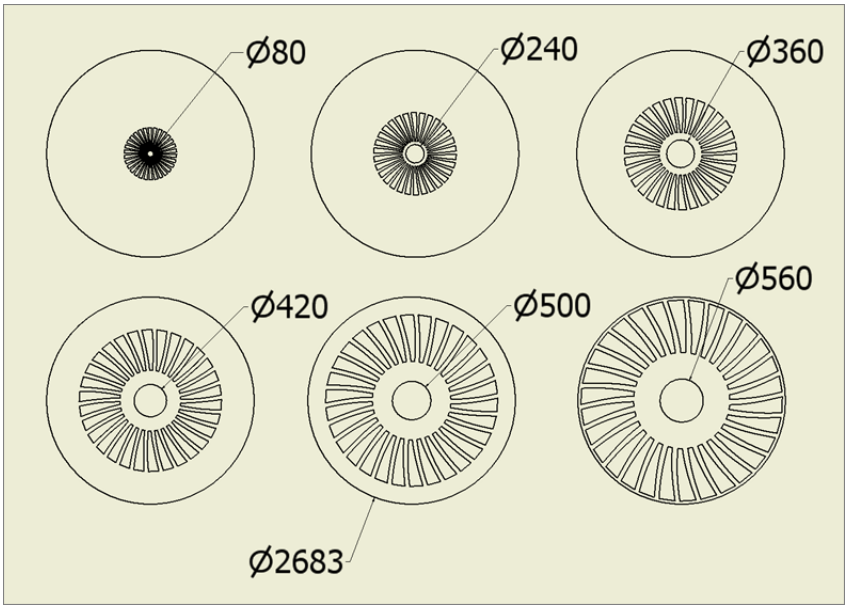

Figure 3.17: Baffle geometries.

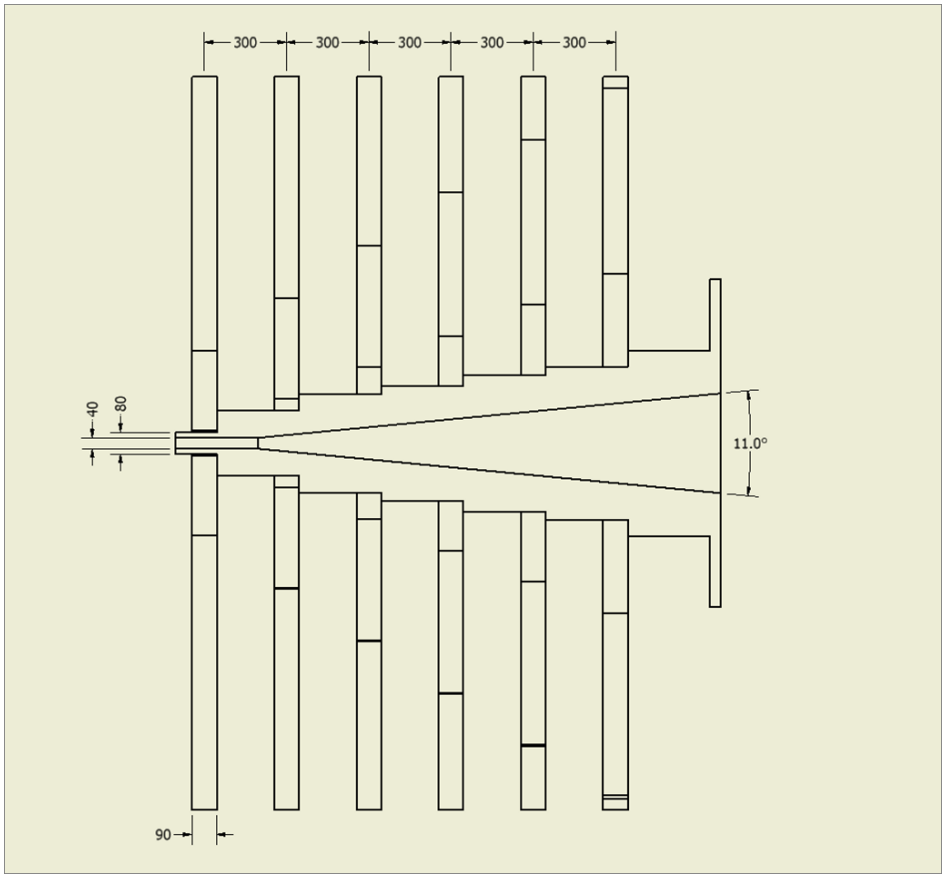

Figure 3.18: Baffle assembly and stepped shaft cross section.

Chapter 4

Concluding Remarks

4.1 Collaboration

The collaboration is quite diverse, including experts of precise parity experiments such as Qweak, G_0, HAPPEX, SLAC E158. We also have groups with the experience to develop and build the necessary hardware. Theoretical support for PVDIS is being provided by collaborators J. Erler and M. Ramsey-Musolf.

4.2 Synergy with Other Proposals

There is significant overlap between the PVDIS and Moller experimental collaborations. This ensures ample expertise in the special issues related to parity experiments. The polarimeters will be shared by both experiments. Since the total fractional error for PVDIS is 0.6%, the demands on polarimetry are more severe. However, since the Moller experiment needs to be strictly statistics limited, our specified precision of 0.4% is very useful for them.

The SIDIS collaboration is also submitting a proposal using the solenoid to make coincidence measurements with a polarized ^{3}He target. While there are significant differences in the configurations for PVDIS and SIDIS, much of the hardware is shared. If both proposals are approved, we plan to work closely together on both experiments.

4.3 Beam Request

For the deuterium data, we have based our sensitivity on 180 days of production running at 50 μA, with 1/3 of the data at 6.6 GeV and the rest at 11 GeV. Approximately 27 additional days, run at various currents, will be required for checkout and calibrations. An additional 18 days will be required at 4.4 GeV and 50 μA for radiative correction measurements. The total beam request at all energies for the deuterium measurement is 225 days, with about 25 of those days run mostly at reduced beam currents.

For the hydrogen measurement, 90 days are needed for production data at 11 GeV, about 9 days are required at 4.4 GeV to control radiative corrections and another 14 days will be required for calibration. The running time requested for hydrogen totals to 113 days.

In the future, we would also anticipate requesting an additional comparable run for a heavy nucleus such as Pb.

4.4 Cost and Schedule

We are preparing a preliminary cost estimate for the project. However, it is already clear that significant funds will be required from several agencies. We plan to seek funding from the US DOE, NSF, and international sources. As emphasized earlier, this project has been listed in the Fundamental Symmetries initiative in the NSAC Long Range Plan, and has been included in the Plan's 10 year funding profile.

Assuming that we receive the endorsement of the JLab PAC, we will request a technical review by the end of 2010 so that we can start seeking funding from the agencies early in 2011. The goal is to start construction by 2013 and schedule installation for 2016.

4.5 Assignment of Tasks

We list below key subsystems and institutions who are interested in design, construction and implementation of them. Note that these are not firm or binding responsibilities, but simply the current thinking of the collaboration given each institution's current interests and past experience. As emphasized earlier, we expect the collaboration to expand should we receive PAC approval.

- **Polarized source:** *UVa, JLab*
- **Cryo Target:** *JLab, MissSt*
- **Magnet:** *UMass, JLab, MIT, ANL*
- **Baffles:** *Longwood*
- **Tracking Detectors:** *UVa, Seoul Nat'l, Kentucky, William and Mary, MissSt, China Collaboration (USTC, Beijing, China IAE, Lanzhou, Tsinghua, Huangshan), Italian Collaboration (3 Institutions INFN Roma, INFN Catania)*
- **Gas Cerenkov:** *Temple, ANL, Ohio*
- **Shower:** *William and Mary, Syracuse, UMass, Rutgers, VaTech*
- **Electronics:** *JLab*
- **Polarimetry:** *UVa, Syracuse, JLab, CMU, ANL, MissSt*
- **Data Acquisition:** *UVa, JLab, LANL, Ohio, LaTech*
- **Simulations:** *Longwood, JLab, UVa, LaTech*

Appendix A

Systematic Corrections

A.1 Kinematic Reconstruction

In order to reconstruct the kinematic quantities of interest, i.e. Q^2, x_{Bj}, etc, we will need precise measurements of the beam energy E_b, the scattering angle θ and the final-state energy E' as well as having good PID for the scattered particle. The PID is provided by the electromagnetic calorimeter (ECAL) shower and preshower data combined with the Cherenkov detector data.

The general strategy is to rely on the excellent knowledge of E_b and to calibrate the apparatus with elastic scattering. The scattering angle may be reconstructed with ~ 0.5 mrad accuracy using the high-resolution GEM tracking information and precise measurements of the detector positions. We plan to map out the magnetic field in the tracking area, for the momentum reconstruction. Additionally, we plan to use the elastic scattering off hydrogen at beam energies of 4.4 and 6.6 GeV to calibrate the measurements of the momentum and Q^2. With the expected spectrometer resolution, at 4.4 GeV the elastic peak will be separated from the inelastic background, with a contamination from the latter of about 5%. At 6.6 GeV the contamination will be about 25%. Since the expected rate at the full luminosity will be high (50 kHz at 4.4 GeV and 4 kHz at 6.6 GeV) further optimization of the calibration conditions are possible, for example using thinner targets or running at a low current. Comparing the elastic peaks at two beam energies will allow to cross-check both the momentum and the angle scales, and calibrate the Q^2 measurement to a 0.2% accuracy.

Several options exist to increase the accuracy further. They will be considered at the next stage of development. For a better selection of the elastic events one can detect the recoil proton, which, for the given electron kinematics, mostly stays within the acceptance of the spectrometer. For this, we will need to be able to rotate the baffle wheels in order to allow positively charged particles to come through. Another possibility is to make calibration runs without the baffles, and at much lower luminosity. Note that the beam position and current monitors are already being upgraded to achieve good accuracy (better than 0.1 mm in position) at very low currents (down to 0.1 nA).

Measurements of beam energy E_b to better than 10^{-3} accuracy are routine at JLab,

and with the upgrade of the ARC energy measurement apparatus for the 11 GeV era, which is already foreseen in Hall A, we should continue to have this accuracy.

The ECAL can be initially calibrated with the elastic scattering on hydrogen, and then continuously monitored and recalibrated using the main data set of DIS electrons and the momentum reconstruction by the spectrometer.

A.2 Radiative Corrections

A.2.1 Electromagnetic (EM) Radiative Correction

In the scattering process both the incident and the scattered electrons can emit photons, and the kinematics (Q^2, W) at the reaction vertex is different from that reconstructed from the beam energy and the measured momentum and angle of the scattered electron. Consequently, when we extract cross sections and asymmetries from the measured values there are electromagnetic radiative corrections to be made. The theory for the EM radiative corrections is well developed [48] and the corrections can in principle be calculated. However, an uncertainty to this correction arises from the uncertainty of the input structure functions, in particular those from the resonance regions.

Figure A.1 shows the region of covered Q^2 and W for the reconstructed kinematics of events in the acceptance (blue), and the region containing the true vertex kinematics for those events (red). About 10% of events will come from the resonance region due to internal and external Bremsstrahlung. We anticipate that A/Q^2 will be roughly constant everywhere. However, the Q^2 and the effective initial state polarization are altered for radiative processes. The size of the full radiative correction can be as large as 6% of the measured asymmetry. To limit the uncertainty of EM radiative corrections to a tolerable level, we plan to measure the PV asymmetry in the lower W and Q^2 region using lower beam energies. Using about 10% of the DIS production time, the error on the radative corrections can be limited to an acceptable ($< 0.3\%$) level.

A.2.2 Electroweak Radiative Correction

The products of weak charges $C_{1,2u(d)}$ given by Eq. (B.7-B.10) are valid only for the case in which there is no electroweak radiative correction. With this correction they are given by

$$C_{1u} = \rho'[-\frac{1}{2} + \frac{4}{3}\kappa' \sin^2(\theta_W)] + \lambda_{1u} \quad \text{(A.1)}$$

$$C_{1d} = \rho'[\frac{1}{2} - \frac{2}{3}\kappa' \sin^2(\theta_W)] + \lambda_{1d} \quad \text{(A.2)}$$

$$C_{2u} = \rho[-\frac{1}{2} + 2\kappa \sin^2(\theta_W)] + \lambda_{2u} \quad \text{(A.3)}$$

$$C_{2d} = \rho[\frac{1}{2} - 2\kappa \sin^2(\theta_W)] + \lambda_{1d} \quad \text{(A.4)}$$

Figure A.1: Region of phase space containing the vertex kinematics (red) compared to that covered by the reconstructed kinematics (blue) for the proposed measurement.

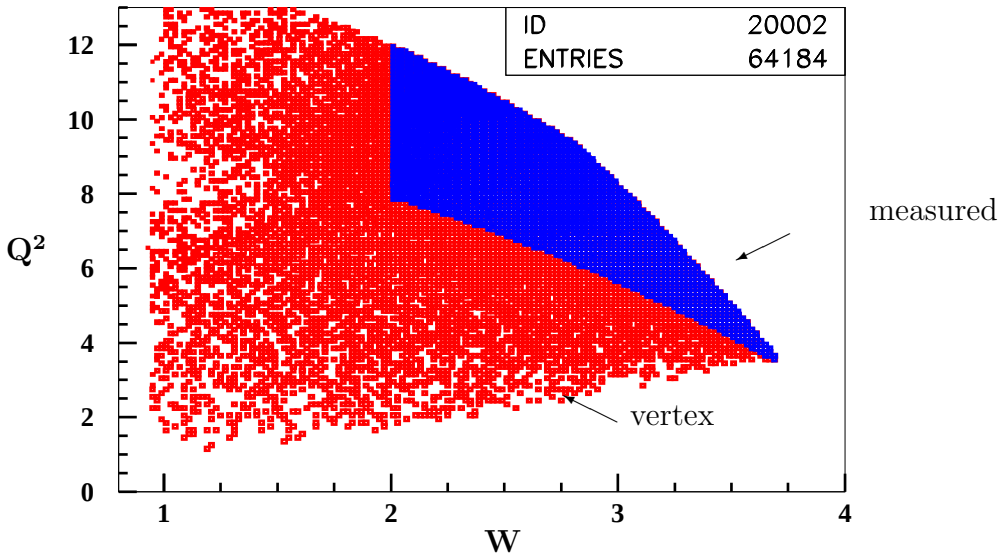

The electroweak radiative correction is well determined in the Standard Model. Standard Model electroweak radiative corrections to $C_{1,2u(d)}$ have been calculated [49] and are relatively small. The corrections modify the ρ, κ, and λ parameters from their tree level values $\rho - \rho' = \kappa = \kappa' = 1$ and $\lambda_{1u} = \lambda_{1d} = \lambda_{2u} = \lambda_{2d} = 0$. A recent evaluation [50, 51] gives $\rho' = 0.9881$, $\kappa' = 1.0027$, $\rho = 1.0011$, $\kappa = 1.0300$, $\lambda_{1d} = -2\lambda_{1u} = 3.7 \times 10^{-5}$, $\lambda_{2u} = -0.0121$, $\lambda_{2d} = 0.0026$. Also $\sin^2\theta_W = 0.2312$, where we are using the $\overline{MS}$ scheme.

The above values are computed for $Q^2 = 0$. We are presently calculating the Q^2-dependent terms. We anticipate that the changes, although critical at the proposed level of precision, will be smaller in size than those for Møller scattering.

Appendix B

Higher Twists

B.1 Introduction

This appendix is a summary on the workshop on higher twist held in Madison, Wisconsin in June, 2009. Talks ere presented by P. Souder, M. Ramsey-Musolf, J Blumlein, P. Mulders, G. Pas, A Belitski, P Reimer, C Keppel, A Deur, and T Hobbs. The conclusion of the workshop was that the physics of higher twist is an important topic in PVDIS. The justification for this conclusion is given in detail, and will form the basis of the updated SOLID proposal.

The main points are as follows:

1. Only quark-quark correlations can produce higher twist effects in the dominant axial-electron a_1 contribution to A_{PV}, as is explained in Section B.2.3. To our knowledge, PVDIS is the only experimental observable that can isolate this important class of higher twist terms. Uncertainties in the physics of $R^{\gamma Z}$ cannot induce an uncertainty in this term as explained in Section B.2.4. These properties follow directly from the elementary phenomenology PVDIS, which is discussed in detail in Section B.2.

2. Higher twist is discussed in Section B.3 in terms of the OPE. We point out that the higher twist contributions to the small vector-electron a_3 term can be unambiguously determined from data on neutrino and parity-conserving electron scattering, as explained in Section B.3.1.

3. In Section B.3.2, we argue that the target mass corrections are under control.

4. Published fits of higher twist contributions to experimental data are discussed in Section B.4. A recent analysis (not discussed at the workshop) shown in Figure B.7, provides information on higher twist in neutrino scattering that is of suitable precision for our experiment.

Other relevant points were discussed. In Section B.5, various theoretical models for higher twist are discussed, and additional data and fits are given in Appendix A. Recent progress in the theory of higher twist is discussed in Section B.6.

In Section B.7.1, possible contributions to the asymmetry due to charge symmetry violation (CSV) are discussed. Section B.7.2 presents our method for distinguishing the various hadronic and Standard Model effects from our data. Finally, in Section B.8, we discuss the possibility of increasing our ability to untangle the physics by using data at forward angles obtained with the SHMS spectrometer in Hall C.

The main points of the workshop are summarized in Section B.9 and the main conclusions are given in Section B.10.

B.2 DIS Phenomenology

In order to make a precise comparison of the data with theory, a careful treatment of the asymmetry must be used [2]. In the approximation that one photon or Z is exchanged, the cross section for scattering polarized electrons from unpolarized nuclei can be written formally in terms of products of hadronic and leptonic tensors.

$$\frac{d^2\sigma}{d\Omega dE'} = \frac{\alpha^2}{Q^4}\frac{E'}{E}\left(L^{\gamma}_{\mu\nu}W^{\mu\nu}_{\gamma} + \frac{G_F}{4\sqrt{2}\pi\alpha}L^{\gamma Z}_{\mu\nu}W^{\mu\nu}_{\gamma Z}\right).$$

In the Standard Model, the lepton tensor for the interference term is related to the electromagnetic lepton tensor

$$L^{\gamma}_{\mu\nu} = 2(l_\mu l'_\nu + l'_\mu l_\nu - l\cdot l' g_{\mu\nu} + i\lambda\varepsilon_{\mu\nu\alpha\beta}l^\alpha l'^\beta)$$

by

$$L^{\gamma Z}_{\mu\nu} = (g^e_V + \lambda g^e_A)L^{\gamma}_{\mu\nu}$$

where λ is 1 (-1) for positive (negative) helicity of the initial lepton beam. Here we have used the conventions that $g^e_A = 1$, $g^e_V = -1 + 4\sin^2\theta_W$, $g^u_A = 1/2$, and $g^u_V = -1/2 + (4/3)\sin^2\theta_W$, etc.

The hadronic tensors can be expanded in terms of currents:

$$W^{\gamma(\gamma Z)}_{\mu\nu} = \frac{1}{2M}\sum_X\{\langle X|J^{\gamma(Z)}_\mu|N\rangle^*\langle X|J^{\gamma}_\mu|N\rangle$$

$$+ \langle X|J^{\gamma}_\mu|N\rangle^*\langle X|J^{\gamma(Z)}_\mu|N\rangle\}(2\pi)^2\delta(P_X - p - q). \quad \text{(B.1)}$$

Here $J^{\gamma(Z)}_\mu$ is the hadronic electromagnetic (weak) current and M is the nucleon mass, and N is the target nucleus.

The electromagnetic hadronic current is purely vector, but the weak current has both vector and axial vector components:

$$J^Z_\mu = J^{(V)Z}_\mu + J^{(A)Z}_\mu.$$

Thus we can decompose the tensors:

$$W^{(VV)\gamma(\gamma Z)}_{\mu\nu} = \frac{1}{2M}\sum_X\{\langle X|J^{(V)\gamma(Z)}_\mu|N\rangle^*\langle X|J^{\gamma}_\mu|N\rangle + HC\}(2\pi)^2\delta(P_X - p - q)$$

and

$$W_{\mu\nu}^{(AV)\gamma Z} = \frac{1}{2M}\sum_X \{\langle X|J_\mu^{(A)Z}|N\rangle^*\langle X|J_\mu^\gamma|N\rangle + HC\}(2\pi)^2\delta(P_X - p - q)$$

In particular,

$$W_{\mu\nu}^\gamma = W_{\mu\nu}^{(VV)\gamma};\quad W_{\mu\nu}^{\gamma Z} = W_{\mu\nu}^{(VV)\gamma Z} + W_{\mu\nu}^{(AV)\gamma Z}$$

This decomposition is especially useful since the vector currents are conserved (CVC).

By using Lorentz invariance, the hadronic current can be further decomposed into three structure functions F_i^j where $j = \gamma$ is the purely electromagnetic tensor and $j = \gamma Z$ is the interference tensor:

$$W_{\mu\nu}^{(VV)j} = -\frac{g_{\mu\nu}}{M}F_1^j + \frac{p_\mu p_\nu}{Mp\cdot q}F_2^j$$

for the vector hadronic part and

$$W_{\mu\nu}^{(VA)\gamma Z} = \frac{i\varepsilon_{\mu\nu\alpha\beta}p^\alpha p^\beta}{2Mp\cdot q}F_3^{\gamma Z}$$

for the term with the axial current. The F_i^j are functions of x and Q^2 only. They do not depend on the kinematic variable y, which may then be used to help separate the different structure functions.

Since in the naive parton model the Callan-Gross relation $F_2^j = 2xF_1^j$ holds, it is convenient to define two new combinations of the structure functions

$$F_T^j \equiv 2xF_1^j;\quad F_L^j \equiv r^2 2xF_2^j - F_T^j$$

where

$$r^2 = 1 + \frac{Q^2}{\nu^2} = 1 + \frac{4M^2x^2}{Q^2}. \tag{B.2}$$

Then the Callan-Gross relation is then simply $F_L^i \to 0$. The ratio R^j, which is defined by

$$R^{\gamma(\gamma Z)} \equiv \frac{F_L^{\gamma(\gamma Z)}}{F_T^{\gamma(\gamma Z)}} = \frac{\sigma_L^{\gamma(\gamma Z)}}{\sigma_T^{\gamma(\gamma Z)}} = r^2\frac{F_2^{\gamma(\gamma Z)}}{F_1^{\gamma(\gamma Z)}} - 1$$

is also commonly used.

The parity-violating asymmetry

$$-A^{LR} = A^{PV} = \frac{\sigma_R - \sigma_L}{\sigma_R + \sigma_L} \sim \frac{\tilde{A}_Z}{A_\gamma} \tag{B.3}$$

in full generality may be written in terms of structure functions

$$A^{PV} = -\left(\frac{G_F Q^2}{4\sqrt{2}\pi\alpha}\right)\frac{g_A^e(2xyF_1^{\gamma Z} - 2[1 - 1/y + xM/E]F_2^{\gamma Z}) + g_V^e x(2-y)F_3^{\gamma Z}}{2xyF_1^\gamma - 2[1 - 1/y + xM/E]F_2^\gamma}.$$

A more convenient expression is

$$A^{PV} = -\left(\frac{G_F Q^2}{4\sqrt{2}\pi\alpha}\right)\left[g_A^e Y_1 \frac{F_1^{\gamma Z}}{F_1^\gamma} + \frac{g_V^e}{2} Y_3 \frac{F_3^{\gamma Z}}{F_1^\gamma}\right] = -\left(\frac{G_F Q^2}{4\sqrt{2}\pi\alpha}\right)(Y_1 a_1 + Y_3 a_3) \qquad \text{(B.4)}$$

where we have chosen to use F_1^γ for the denominator. Similar expressions are found where the denominator is F_2^γ.

The Y_i are functions of the kinematic variable $y = \nu/E$ and the ratios of structure functions $R^j(x, Q^2)$:

$$Y_1(x, y, Q^2) = \frac{1 + (1-y)^2 - y^2(1 - r^2/(1+R^{\gamma Z})) - 2xyM/E}{1 + (1-y)^2 - y^2(1 - r^2/(1+R^{\gamma})) - 2xyM/E}\left(\frac{1+R^{\gamma Z}}{1+R^\gamma}\right) \qquad \text{(B.5)}$$

$$Y_3(x, y, Q^2) = \frac{1 - (1-y)^2}{1 + (1-y)^2 - y^2(1 - r^2/(1+R^{\gamma})) - 2xyM/E}\left(\frac{r^2}{1+R^\gamma}\right) \qquad \text{(B.6)}$$

The above expressions are quite general.

B.2.1 QCD and the Naive Quark Parton Model

The proper theory of hadronic structure is QCD. At high energies, a useful expansion of QCD is based on the quark-parton model (QPM). In the limit of large Q^2, the structure functions can be described by parton distribution functions (PDF's) functions $f_i(x)$ ($\overline{f}_i(x)$), which are the probabilities that the i^{th} quark (antiquark) carries a fraction x of the nucleon momentum. With the definitions $f_i^\pm = f_i \pm \overline{f}_i$, $y = \nu/E$, the structure functions are given by

$$F_1^\gamma = \frac{1}{2}\sum_i Q_i^2(f_i(x) + \overline{f}_i(x)); \quad F_2^\gamma = 2xF_1^\gamma$$

$$F_1^{\gamma Z} = \sum_i Q_i g_V^i(f_i(x) + \overline{f}_i(x)); \quad F_2^{\gamma Z} = 2xF_1^{\gamma Z}$$

$$F_3^{\gamma Z} = 2\sum_i Q_i g_A^i(f_i(x) - \overline{f}_i(x)).$$

In order to account for possible violations of the Standard Model, is is convenient to express the parity-violating part of the electron-hadron interaction in terms of phenomenological four-fermion contact interactions. couplings C_{ij}

$$\mathcal{L}^{PV} = \frac{G_F}{\sqrt{2}}[\overline{e}\gamma^\mu\gamma_5 e(C_{1u}\overline{u}\gamma_\mu u + C_{1d}\overline{d}\gamma_\mu d) + \overline{e}\gamma^\mu e(C_{2u}\overline{u}\gamma_\mu\gamma_5 u + C_{2d}\overline{d}\gamma_\mu\gamma_5 d)]$$

with additional terms as required for the heavy quarks. Here C_{1j} (C_{2j}) gives the vector (axial-vector) coupling to the j^{th} quark. For the Standard Model:

$$C_{1u} \;=\; g_A^e g_V^u \approx -\frac{1}{2} + \frac{4}{3}\sin^2\theta_W \approx -0.19 \qquad \text{(B.7)}$$

$$C_{1d} = g_A^e g_V^d \approx \frac{1}{2} - \frac{2}{3}\sin^2\theta_W \approx 0.34 \quad \text{(B.8)}$$

$$C_{2u} = g_V^e g_A^u \approx -\frac{1}{2} + 2\sin^2\theta_W \approx -0.030 \quad \text{(B.9)}$$

$$C_{2d} = g_V^e g_A^d \approx \frac{1}{2} - 2\sin^2\theta_W \approx 0.025 \quad \text{(B.10)}$$

The numerical values include electroweak radiative corrections.

In the naive QPM, $F_L^j = 0$, so

$$Y_1 \approx 1; \quad Y_3 \approx \frac{1-(1-y)^2}{1+(1-y)^2} \equiv f(y) \quad \text{(B.11)}$$

and

$$a_1(x) = g_A^e \frac{F_1^{\gamma Z}}{F_1^\gamma} = 2\frac{\sum_i C_{1i} Q_i f_i^+(x)}{\sum_i Q_i^2 f_i^+(x)}; \quad a_3(x) = \frac{g_V^e}{2}\frac{F_3^{\gamma Z}}{F_1^\gamma} = 2\frac{\sum_i C_{2i} Q_i f_i^-(x)}{\sum_i Q_i^2 f_i^+(x)}$$

For isoscalar targets such as the deuteron, the structure functions almost cancel and we have

$$a_1^D(x) = \frac{6}{5}(2C_{1u} - C_{1d})\left(1 + \frac{2s^+}{u^+ + d^+}\right); \quad a_3^D(x) = \frac{6}{5}(2C_{2u} - C_{2d})\left(\frac{u^- + d^-}{u^+ + d^+}\right) + \ldots \quad \text{(B.12)}$$

For $x > 0.4$, only valence quarks are important, and the expressions for a_1 and a_3 become constants. Then the asymmetry becomes

$$A_{PV} = -\frac{G_F Q^2}{\sqrt{2}\pi\alpha}\left(\frac{9}{20}\right)\left[1 - \frac{20}{9}\sin^2\theta_W + (1 - 4\sin^2\theta_W) f(y)\right]. \quad \text{(B.13)}$$

B.2.2 From the QPM to QCD

The QPM serves as a suitable starting point for rigorous QCD. However, there are two additional steps.

1. Apply the DGLAP equations to the PDF's. This is the leading-twist approximation.

2. Add higher twist, or power corrections. These terms are based on the Operator Product Expansion (OPE).

The first step has two consequences:

1. The PDF's become functions of Q^2.

2. The Callan-Gross relation is violated, and $R^{(\gamma(\gamma z)} \approx 10 - 20\%$ for JLab kinematics. However, in this approximation, R can be determined from the usual PDF's, with

significant contributions from both quarks and gluons as given in the following equation:

$$F_L(x,Q^2) = \frac{\alpha(Q^2)}{2\pi}x^2\int_x^1 \frac{dy}{y^3}\left[\frac{8}{3}F_2(y,Q^2) + 4N_f g(y,Q^2)(1-\frac{x}{y})\right]. \tag{B.14}$$

Indeed, data on R provides information on the gluonic PDF.

Another point is that the DGLAP evolution of the PDF's can be taken to fairly high order, even NNNLO. However, to get a consistent picture involving, for example, higher twist and target mass corrections, everything must be done to the same order, as was emphasized many times at the workshop. Corrections that may appear as DGLAP at higher order may be higher twist in a lower order computation. The higher twist corrections also contribute to R.

B.2.3 Q^2 Dependence and Quark-Quark Correlations

The term $Y_1 a_1^D$ involves only conserved vector currents. As a consequence, we can make a strong statement about possible hadronic corrections that were addressed by Bjorken, Wolfenstein and Derman [24, 25, 26] shortly after the data of Prescott, et al. were published. Going back to the hadronic tensor in terms of currents, we can write $Y_1 a_i^D$ as

$$Y_1 a_1^D \propto \frac{L^{\mu\nu}_{\gamma Z}\sum_X\{\langle X|J^{(V)Z}_\mu|\rangle^*\langle X|J^\gamma_\nu|D\rangle + H.C.\}(2\pi)^3\delta(P_X-p-q)}{L^{\mu\nu}_{\gamma}\sum_X\{\langle X|J^{\gamma}_\mu|\rangle^*\langle X|J^\gamma_\nu|D\rangle + H.C.\}(2\pi)^3\delta(P_X-p-q)}.$$

Next, we decompose the electromagnetic current

$$J^{em}_\mu = \frac{2}{3}\overline{u}\gamma_\mu u - \frac{1}{3}\overline{d}\gamma_\mu d$$

in terms of isospin

$$V_\mu = (\overline{u}\gamma_\mu u - \overline{d}\gamma_\mu d); \quad S_\mu = (\overline{u}\gamma_\mu u + \overline{d}\gamma_\mu d)$$

and define

$$\langle VV\rangle = L^{\mu\nu}_\gamma \sum_X \langle X|V_\mu|D\rangle^*\langle X|V_\nu|D\rangle(2\pi)^3\delta(P_X-p-q)$$

with similar expressions for $\langle SS\rangle$ and $\langle SV\rangle$ The vector part of the weak current can also be treated in this way.

Then the asymmetry for an isoscalar target is proportional to

$$Y_1 a_1^D \propto \frac{(C_{1u}-C_{1d})\langle VV\rangle + \frac{1}{3}(C_{1u}+C_{1d})\langle SS\rangle}{\langle VV\rangle + \frac{1}{3}\langle SS\rangle} \tag{B.15}$$

The key here is that the $\langle SV\rangle$ term vanishes in the absence of CSV. Here strange quarks have also been neglected. If $\langle VV\rangle = \langle SS\rangle$, the hadronic corrections, including DGLAP

evolution and higher twist terms, completely cancel. The difference between $\langle VV \rangle$ and $\langle SS \rangle$ can be written

$$\langle VV \rangle - \langle SS \rangle = \langle (V-S)(V+S) \rangle \propto$$
$$L_\gamma^{\mu\nu} \sum_X \{ \langle X|\overline{u}\gamma_\mu u|D\rangle^* \langle X|\bar{d}\gamma_\nu d|D\rangle + H.C. \} (2\pi)^3 \delta(P_X - p - q) \tag{B.16}$$

If this expression vanishes, all of the hadronic corrections in Equation B.15 cancel and the $Y_1 a_1^D$ part of the asymmetry is strictly independent of Q^2. The right hand side of Equation B.16 is a correlation between u and d valance quarks. Thus any Q^2 dependence observed in this term will be a measure of valance quark-quark correlations. The only assumption is that the hadronic vector current is conserved (CVC), which is presupposed by QCD.

The valence PDF's drop rapidly after $x \sim 0.3$. However, the x relevant to the quark-quark correlation function is the sum of the individual x-values of each quark, so it is likely that the correlation function doesn't fall rapidly until $x \sim 0.6$ or so. Thus the ratio of diquarks to single quarks may be strongly enhanced at large x. This argument suggests that the x-dependence of the diquarks could be similar to the observed x-dependence of the higher twist coefficients described below.

Based on the above ideas, one method to remove the contribution of higher twist terms is to do a global fit of the form $D(X) = \alpha(1-x)^n$, where α and n are parameters to be fit. If little Q^2-dependence is observed, n could be fixed in the range $2 < n < 4$. In this scenario, the contribution of the uncertainties in the higher twist coefficient to the high Q^2 point at $x \sim 0.4$ would be small.

In summary, the observation of Q^2-dependent effects would thus be of particular interest [27] in PVDIS because:

1. The experimental signature is especially clean. It is a violation of the QPM prediction that varies with both Q^2 and x. Since the DGLAP evolution cancels in the ratio, there is no uncertainty associated with the order to which the evolution is performed.

2. The theoretical interpretation, namely quark correlations, is well defined and interesting.

B.2.4 Determination of $R^{\gamma Z}$

It was pointed out in the literature [2] that a correction to the $Y_1 a_1$ based on the value of the unmeasured quantity $R^{\gamma Z}$ must be made. At the workshop, we concluded that this is not a problem for the deuteron for two reasons:

1. F_L from Equation B.14 has two contributions, one from gluons, which are flavor-blind, and one from the quarks, which in the case of an isoscalar target, are also flavor-blind. Thus the PDF's cancel. For the proton, which is an isodoublet, a correction to Y_1 based on the PDF's must be made.

2. The argument of Section B.2.3 rules out the possibility that hadronic structure other than quark-quark higher twist terms can alter the quantity $Y_1 a_1$.

At the workshop, we also noted that for neutrino scattering, F_L^ν also has an axial-vector axial-vector piece that would result in PCAC terms. For A^{PV}, the relevant F_L^j are all vector.

B.3 Higher Twist and the Operator Product Expansion

A useful formalism for discussing higher twist is the OPE analysis of Jaffe and Soldate [28, 29] in which the twist-4 ($\sim 1/Q^2$) contributions are expressed in terms of a set of symmetric, traceless, and derivative-free operators. The QCD equations of motion are used to eliminate those operators that arise that do not satisfy these conditions. There are other useful formalisms for computing higher twist, such as that developed by Shuryak and Vainshtein [52, 53].

The physics can be illustrated with the Feynman diagrams from Castorina and Mulders and shown in Figure B.1. Diagram (a) is the leading twist. Diagram (b) is a quark-gluon correlation, and diagram (c) is a quark-quark correlation that can contribute to $Y_1 a_1$. Care must be taken because the QCD equations of motion can be used to convert quark-quark correlations into quark-gluon correlations, as illustrated in Figure B.3. The two diagrams are the same, but the one on the left appears to be a quark-quark correlation. However, since the higher twist in $Y_1 a_1$ is a correlation between up and down quarks, the diagrams in Figure B.3 do not apply. For reference, the diagrams in Figure B.2, with the exception of diagram (d), are contributions to the DGLAP evolution. The quark-quark correlations in $Y_1 a_1$ come only from the first six operators in Appendix A in Jaffe and Soldate [29] ; the rest of the operators can be expressed as quark-gluon operators. In other treatments of the OPE, quark-gluon correlations can be transformed into transverse momentum.

B.3.1 Physics of $Y_3 a_3^D(x)$

For the contribution to A^{PV} due to $F_3^{\gamma Z}$, there is no CVC theorem to help cancel uncertainties in the structure functions in the asymmetry. Fortunately, the $a_3(x)$ term is small in the Standard Model

$$\frac{a_3(x)}{a_1(x)} \sim 11.5\%$$

so a high precision is not required. The suppression factor is essentially the ratio of electron-Z couplings g_V^e/g_A^e. The proposed Standard Model test comprises of measuring this ratio with a relative error of 5%.

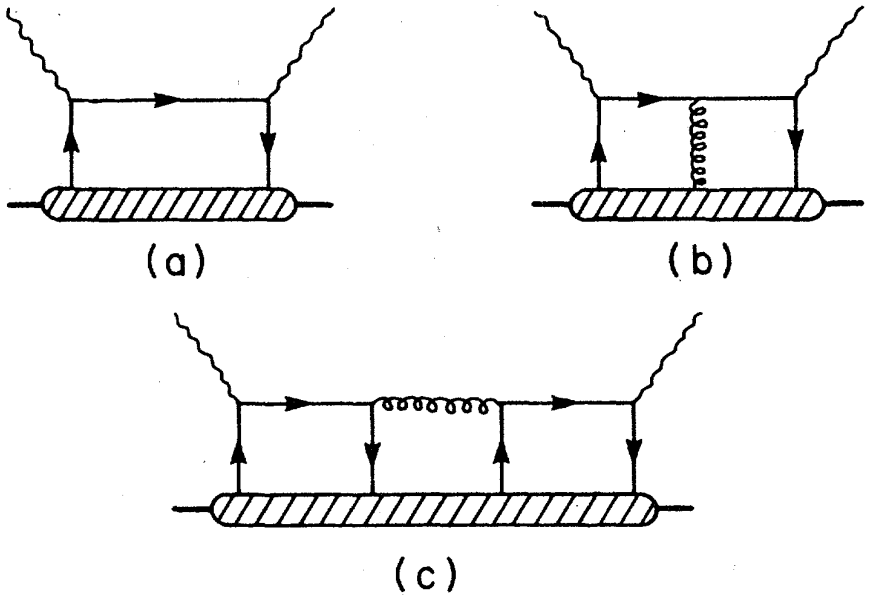

Figure B.1: Comparison of quark-quark correlations and quark-gluon correlations

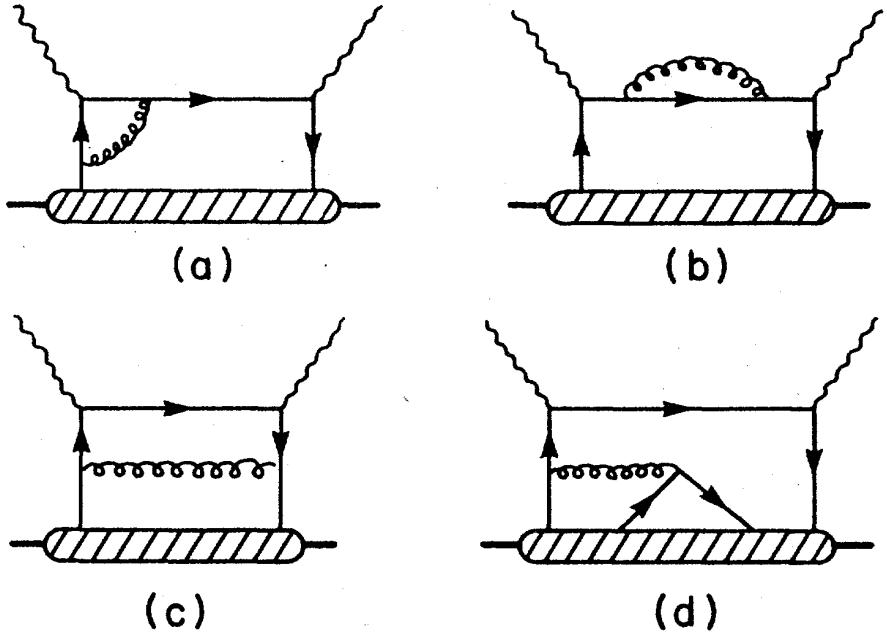

Figure B.2: Diagrams corresponding to DGLAP evolution. The exception is diagram (d), which is a quark-gluon operator.

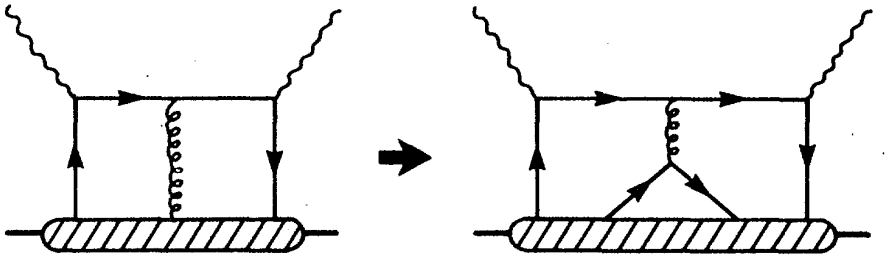

Figure B.3: The QCD equations of motion can be used to convert quark-gluon operators (left) to look like quark-quark correlations (right). However, the resulting diagram does not correspond to any of the first six operators in the Jaffe-Soldate paper.

Another approach, also mentioned by Bjorken, is to note that the axial current is just an isospin rotation of the $\nu - D$ *charge current* interaction

$$F_3^{\gamma Z} = \frac{5}{18} F_3^{\nu}$$

The conclusion of the workshop is that data should be used to estimate the higher twist contributions to the $Y_3 a_3$ term. The structure functions F_3^{ν}, F_L^{γ}, and F_2^{γ} all contribute.

In order to evaluate the empirical approach, we have reviewed data on neutrino scattering, which dominate the errors. The structure functions are extracted from cross sections by using the equation

$$\frac{d^2\sigma}{dxdy} = \frac{G_\mu M E}{\pi} \left[xy^2 F_1 + F_2 \left(1 - y - \frac{Mxy}{2E} \right) \pm F_3^{\nu} xy \left(1 - y/2 \right) \right] \tag{B.17}$$

Charged neutrino scattering has the advantage that the energy of the incident neutrino is given by the total detected energy. From Equation B.17, it is apparent that the cross section is sensitive to F_3 only for large values of y. In order to obtain data on F_3 at our value of x and Q^2, neutrino and antineutrino data with a beam energy of about 15 GeV is required. However, at large y, the experiments are more difficult because the muon has low energy and may be hard to distinguish from hadrons in the shower. This problem is more severe at the low energies we need. As a consequence, large statistics experiments like NuTeV, which were optimized for higher energies, do not provide precise cross sections at the kinematics we need. The MINERVA experiment, however, is optimized for the kinematics we need, so their results will be quite useful.

B.3.2 Target Mass Corrections

Target mass corrections are important for our kinematics. The graph of Figure B.4 illustrates their size relative to higher twist terms. Tim Hobbs presented the effects of target mass corrections for A^{PV}, which were quite small. The experts at the workshop explained that if consistent procedures are used, there is no uncertainty due to the prescription for making target mass corrections.

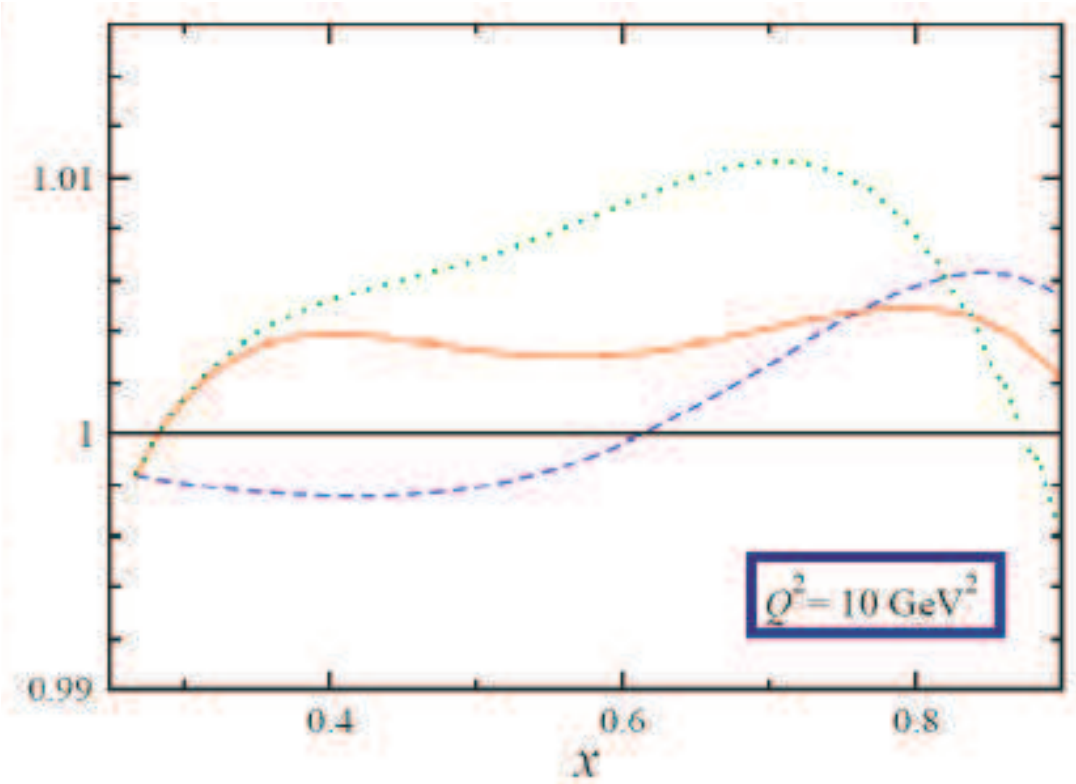

Figure B.4: Target mass corrections to A^{PV} from Hobbs and Melnitchouk.They are smaller than 1%. The curve used to correct the data must be one computed in a manner consistent with the DGLAP evolution. Then the net uncertainty will be negligible.

B.4 Analyses of Higher Twist Data

B.4.1 Data on F_2

We will start with data on F_2, which in terms of experimental precision is the best known. Here the analysis has been performed up to 4^th order in DGLAP. We had a presentation by Blumlein on this analysis. The data are shown in Figure B.5. The deviations from DGLAP evolution are easy to see at large x. Also, significant target mass corrections are apparent. The net higher twist for our kinematics reaches the level of 10%.

Two notations are used. The first is relative and the second as absolute.

$$F_2^\gamma(x,Q^2) = F_2^\gamma(x)(1 + D(x)/Q^2); \quad F_2^\gamma(x,Q^2) = F_2^{(LT)\gamma} + F_2^{(HT)\gamma}$$

Both notations are useful and both will be used. It turns out that the values of the $D(x)$ depend upon how many orders of α_s are taken in the DGLAP evolution of the PDF's. Results presented by Blumlein [54, 39] are shown in Figure B.6.

A similar analysis has been done by the MRST group [16]. At leading order (LO), the higher twist contributions are significant and similar to the results of older analysis [37, 38]. However, as higher orders are taken, NLO, NNLO, and NNNLO, $D(x)$ becomes quite small, especially for $x < 0.4$. The values of D_i for both LO and NNNLO are summarized in Table B.1.

To interpret the size of higher twist terms at large values of x, one must take into account the relationship between W, Q^2 and x:

$$Q^2 = (W^2 - M^2)/(1/x - 1).$$

If $W = 2$ is taken as the threshold for DIS behavior, then there is a threshold Q^2 denoted Q_t^2. Values for Q_t^2 are also given in Table B.1. The maximum size of the higher twist effect that can be measured is thus $D(x)/Q_t^2$, which is also given in Table B.1 as a fraction of $F_2^\gamma(x)$. This fraction is large enough to motivate a measurement only at high x.

The coefficients $D(x)$ increase rapidly at large x, but the main reason is that the PDF's are dropping rapidly. The u quarks fall as $(1-x)^{-2.5}$ and the d quarks as $(1-x)^{-3.5}$. Thus it is useful to look at the absolute higher twist contributions F_2^{HT} shown in Figure B.8 from a thesis on higher twist by Sacco [31]. Here the contribution is relatively flat, dropping at most as $(1-x)^{-1}$ as suggested by Mulders in his talk at this workshop.

Since our measurements of A_{PV} have errors that are roughly constant in x, our sensitivity to higher twist grows by about a factor of 5 over our kinematic range. Thus the data for $0.3 < x < 0.45$, which should have the smallest higher twist contributions, will provide the test for the Standard Model, and the greatest potential to higher twist effects comes from the data for $x > 0.6$.

Data on F_L and F_3 from Sacco's thesis are shown in Figures B.9 and B.10. A recent analysis [36] that does much better for F_3 is shown in Figure B.7. Here, absolute higher twist coefficients are given. Given the precision of this these fits, the contribution to the uncertainty in higher twist terms in the $Y_3 a_3$ term is completely negligible for $x \leq 0.4$ and only about 1% at the highest x bin of 0.7. Unfortunately, the analysis in Figure B.7

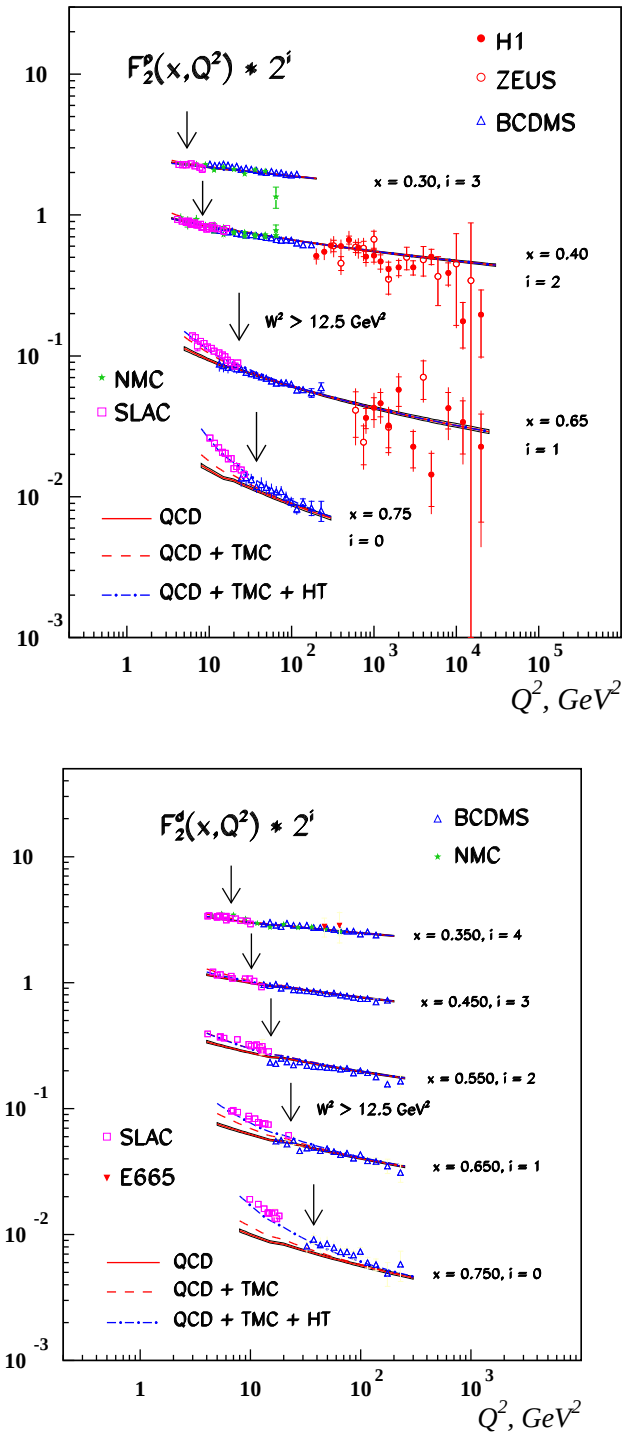

Figure B.5: Higher twist fits from Blumlein and Bottcher

Table B.1: Higher twist coefficients $D(x)$ from Ref. [16].

x	$D(x)$ (LO)	$D(x)$ (NLO)	$D(x)$ (N^{2}LO)	$D(x)$ (%) (N^{3}LO)	Q_t^2 (%)	$D(x)/Q_t^2$ (LO)	$D(x)/Q_t^2$ (N^{3}LO)
0.15	-0.07	-0.03	0.00	0.01	0.5	-14	2
0.25	-0.11	-0.09	-0.04	0.00	1.0	-11	0
0.35	-0.06	-0.13	-0.06	-0.01	1.7	-3.5	-0.5
0.45	0.22	0.01	0.07	.11	2.6	8	4
0.55	0.85	0.40	0.41	0.39	3.8	22	10
0.65	2.6	1.7	1.6	1.4	5.8	45	24
0.75	7.3	5.5	5.1	4.4	9.4	78	47

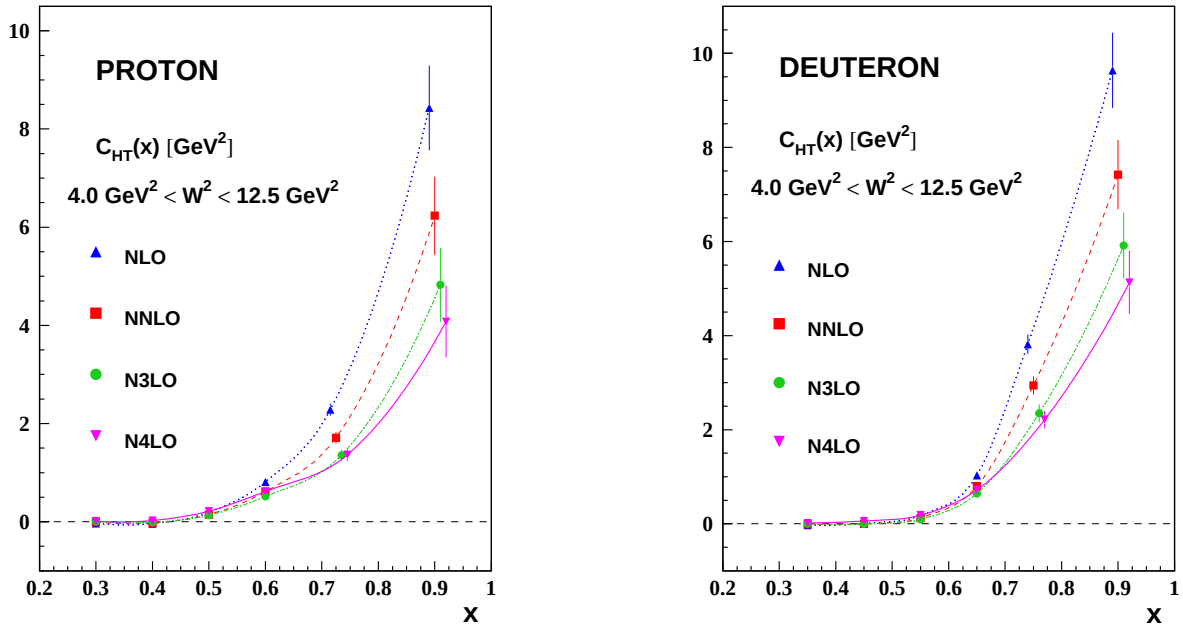

Figure B.6: Relative higher twist fits from Blumlein and Bottcher.

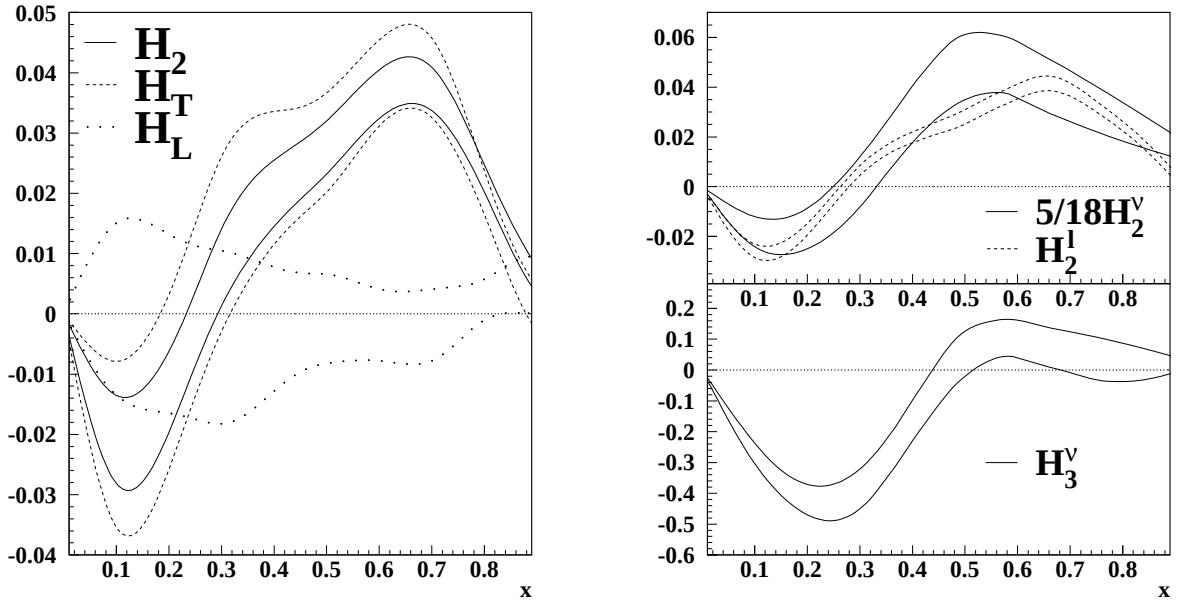

Figure B.7: Data on higher twist from Kulagin, et al. Here *absolute* higher twist coefficients are used.

is only available as a conference proceedings. It would be helpful if other groups doing global analysis could provide fits with similar errors.

B.4.2 Higher Twist Analysis of All Structure Function

The data and MIT bag model predictions from Sacco's thesis mentioned above are presented here (Figs B.8 thru B.12).

B.5 Models

B.5.1 The MIT Bag Model

Estimates of the size of higher twist effects that use the operator product expansion (OPE) in QCD have been made by Castorina and Mulders [30, 55] and Fajfer and Oakes [56]. These papers are based on the work of Jaffe and Soldate. The computation of the matrix elements of these operators is presently less rigorous, and the MIT bag model has been used to make rough estimates.

For their analysis, Castorina and Mulders use a slightly different expression for the asymmetry

$$\frac{A}{Q^2} = a_1 + a_2 f(y) + a_3 g(y) + a_4 f(y) g(y)$$

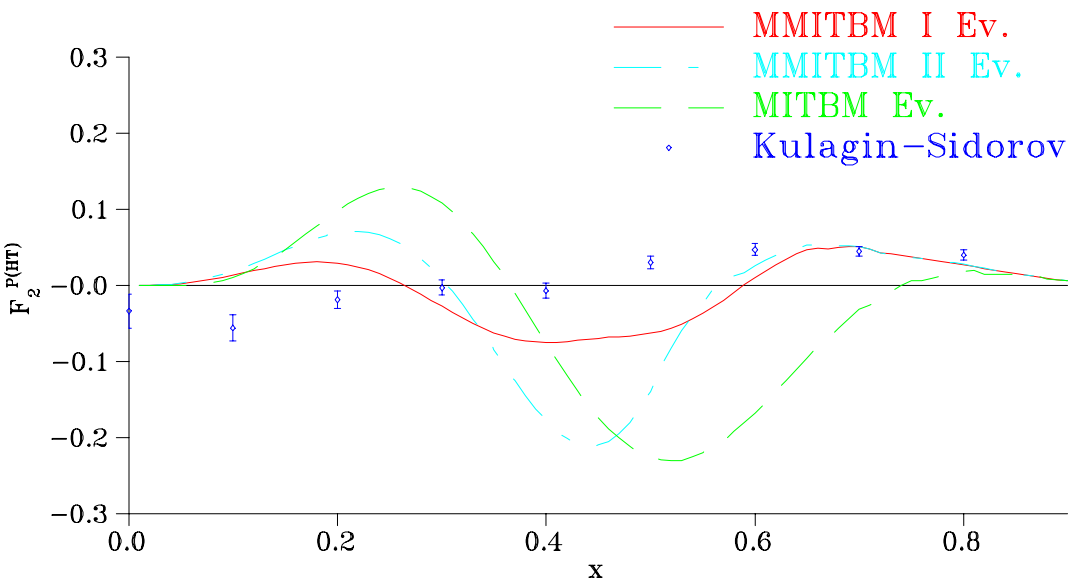

Figure B.8: Data on higher twist for F_2 from Kulagin, et al. with MIT bag model fits from Sacco

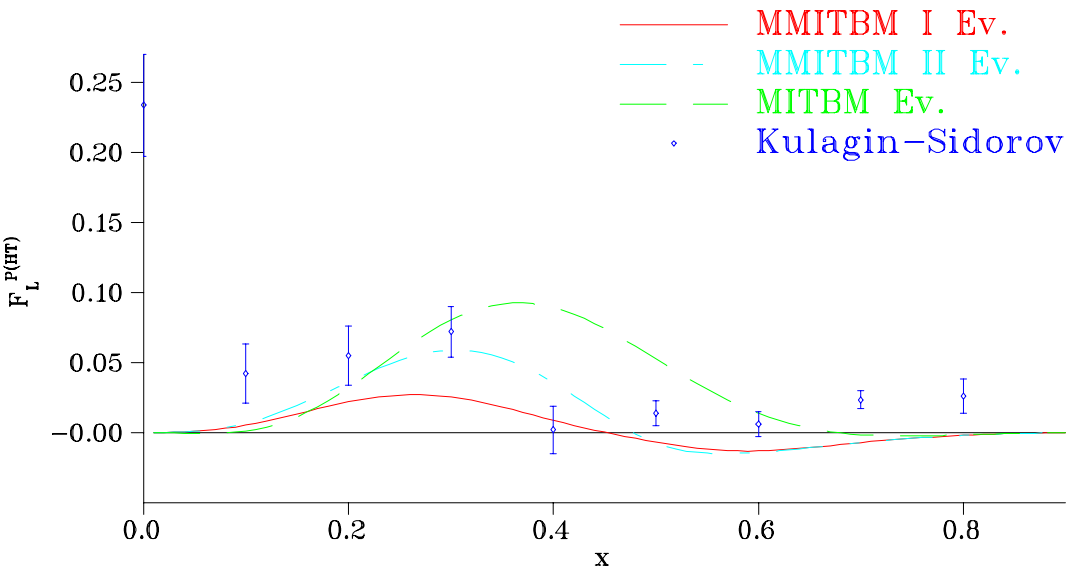

Figure B.9: Data on higher twist for F_L from Kulagin, et al. with MIT bag model fits from Sacco

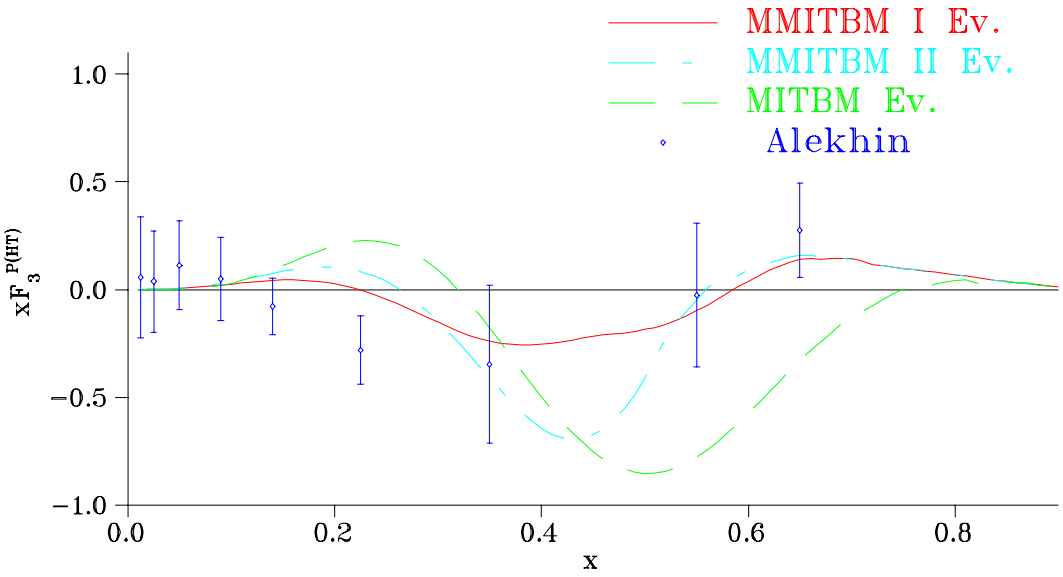

Figure B.10: Data on higher twist for xF_3 from Kulagin, et al. with MIT bag model fits from Sacco

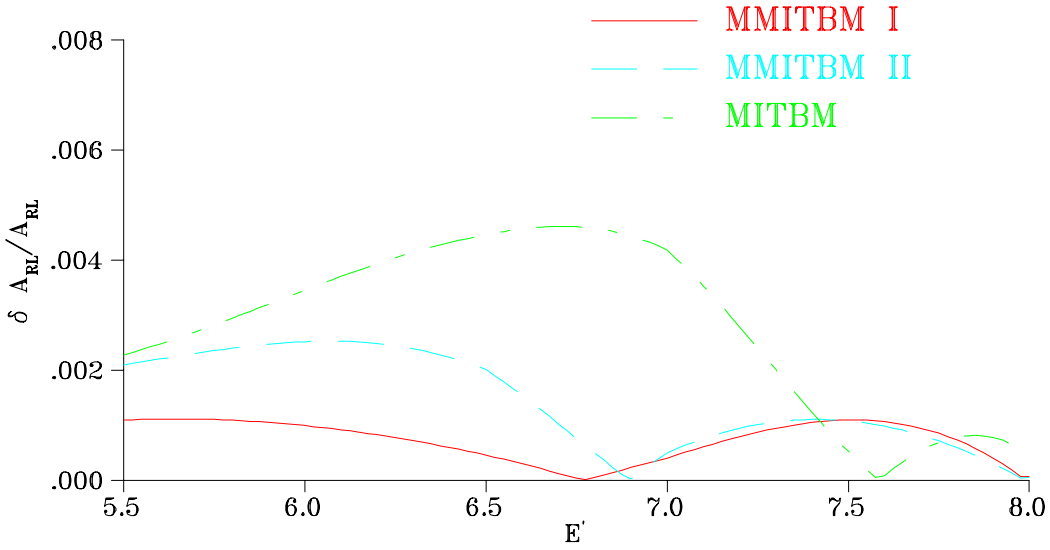

Figure B.11: Contribution to A^{PV} due to quark-gluon operators in the MIT bag model by Sacco.

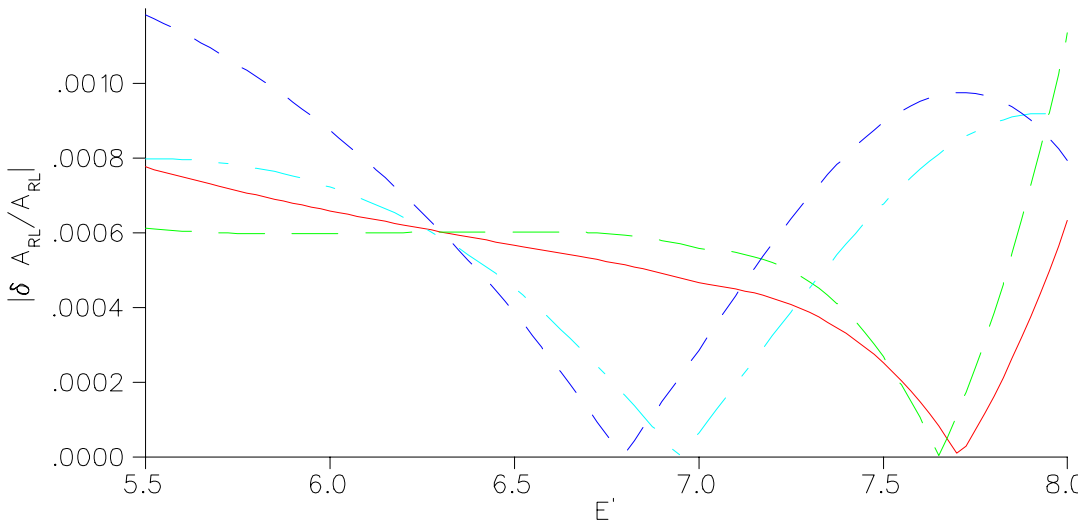

Figure B.12: Contribution to A^{PV} due to quark-quark operators in the MIT bag model by Sacco. The predictions are much smaller than those for the quark-gluon operators.

where

$$f(y) = \frac{1-(1-y)^2}{1+(1-y)^2}; \quad g(y) = \frac{y^2}{1+(1-y)^2}$$

and

$$a_1 = -\frac{G_F}{4\sqrt{2}\pi\alpha}\frac{F_2^{\gamma Z}}{F_2^{\gamma}}$$

$$a_2 = -\frac{G_F}{4\sqrt{2}\pi\alpha}(1-4\sin^2\theta_W)\frac{xF_3^{\gamma Z}}{F_2^{\gamma}}$$

$$a_3 = -\frac{G_F}{4\sqrt{2}\pi\alpha}\left[\frac{2xF_L^{\gamma}F_2^{\gamma Z}}{(F_2^{\gamma})^2} - \frac{2xF_L^{\gamma Z}}{F_2^{\gamma}}\right]$$

$$a_4 = -\frac{G_F}{4\sqrt{2}\pi\alpha}(1-4\sin^2\theta_W)\frac{2xF_L^{\gamma}xF_3^{\gamma Z}}{(F_2^{\gamma})^2}$$

where the approximation

$$\frac{1}{F_2 - g(y)2xF_L} \approx \frac{1}{F_2}\left(1+\frac{g(y)2xF_L}{F_2}\right)$$

is used and F_2 is used as the denominator instead of F_1 as is done in the appendix.

The higher twist contributions are given in terms of constants K_1 and K_2 computed in the MIT bag model;

$$a_1 = -\frac{G_F}{4\sqrt{2}\pi\alpha}\frac{9}{4}\left[1+\frac{1}{Q^2}(-1.4K_1+3.8K_2) - \frac{20}{9}\sin^2\theta_W\right]$$

$$a_2 = -\frac{G_F}{4\sqrt{2}\pi\alpha}\frac{9}{4}\left[1+\frac{1}{Q^2}\left(11.5K_1 - 23.5K_2\right)\right]\left(1-4\sin^2\theta_W\right)$$

$$a_3 = 0$$

$$a_4 = \frac{G_F}{4\sqrt{2}\pi\alpha}\frac{9}{4}\left[\frac{1}{Q^2}\left(4K_1 - 3.5K_2\right)\right]\left(1-4\sin^2\theta_W\right)$$

The most striking result is that $a_3 = 0$. As stated in the paper, this feature arises because the breaking of the Callan-Gross relation ($F_L = 0$) is due to two-quark-gluon operators, which contribute to the γ and γZ terms proportional to the leading twist-2 results. Therefore, there is no contribution to the ratio. This is consistent with the argument due to Bjorken that the only higher twist operators in a_1 involve quark-quark correlations, which are four-quark operators. This result of the calculation is expected to be quite general in the context of QCD.

The analysis of Castorina and Mulders only considered one moment of the higher twist contributions, so it applies only to the average over all x-values. It is quite likely, however, the the effects are larger at larger x. From a theoretical standpoint, the quark-quark correlations add the x-values of each quark, resulting in relatively greater strength at larger x, as suggested by Brodsky [27]. From an empirical standpoint, the higher twist contribution to F_2^γ is observed to be significant only at large x as discussed in Section B.4.

The analysis of Castorina and Mulders only considered the first moments. An analysis was done by Sacco that included the x dependence. Predictions for A^{PV} that are consistent with the observed higher twist in unpolarized structure functions are given in Figure B.11 for quark-gluon operators and in Figure B.12 for the quark-quark correlations. The effects are negligible, especially the quark-quark correlations. The bag model attempts to include the simplest correlations relating to the size of confinement. Clearly we are looking for physics that goes well beyond this model.

B.5.2 The Instanton Model

C. Weiss suggested that care must be taken because of the possibility that the quark-gluon higher twist operators in the $Y_3 a_3$ term might be an order of magnitude larger than the quark-quark correlations. This expectation is based on the existence of a non-perturbative short-distance scale related to the range of chiral-symmetry breaking forces in the QCD vacuum, which may be interpreted phenomenologically as the "size" of the constituent quark [57]. Of course, if the quark-quark correlations are too small for us to observe, this is indeed the case. On goal of the experiment is to provide data relevant to this issue.

The instanton model of the QCD vacuum provides an explicit realization of this scenario and predicts large twist-4 quark-gluon correlation effects in the unpolarized [58] and polarized [59, 57] structure functions, which are in agreement with the higher-twist corrections extracted from a phenomenological analysis of the data." The prediction was that F_L and F_3 would have much large higher twist $1/Q^2$ dependence than F_2. Looking at the data from Figure B.7, higher twist at low x is indeed especially large for F_3. However, in our region of x, the higher twist of $F_3^{\gamma Z}$ is comparable to that of F_2.

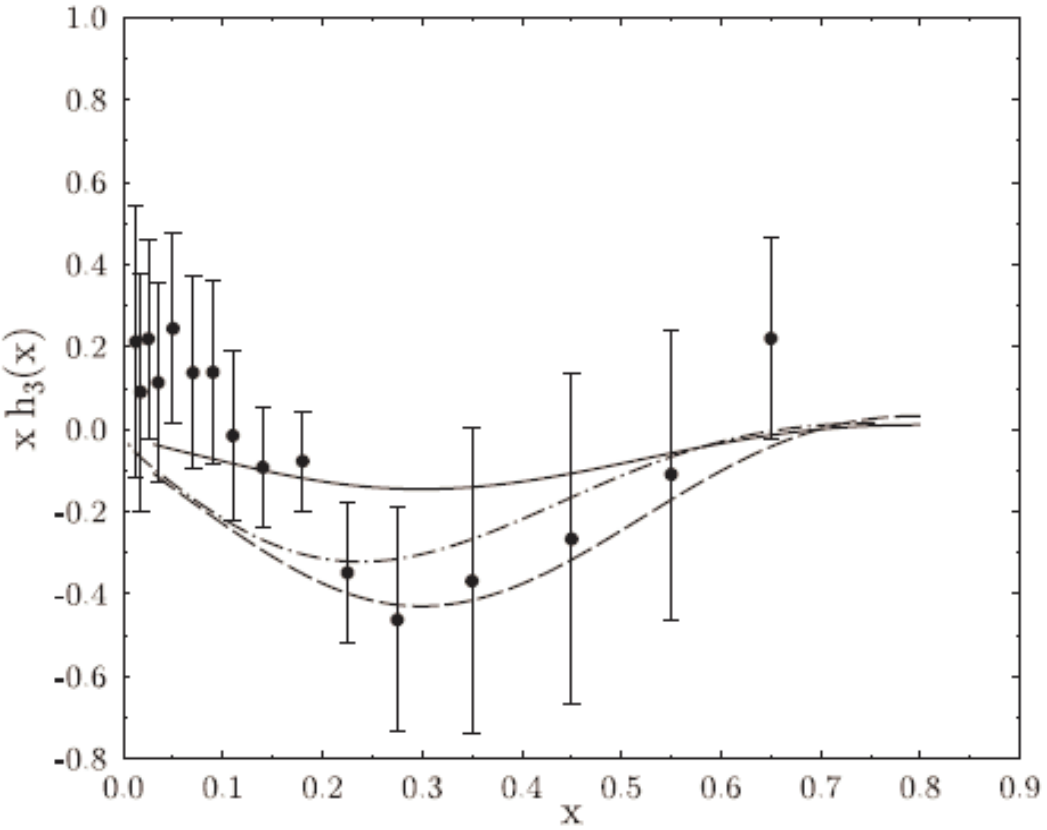

Figure B.13: Predictions of F_3 from a renormalon model.

B.5.3 Renormalons

Renormalon [60] fits to xF_3 data presented at the workshop, which are shown in Figure B.13, have a very different x-dependence than the fit shown in Figure B.7. For $x < 0.5$, the contribution is of opposite sign and much larger. The MIT bag model predictions for xF_3 shown in Figure B.10 are also closer to the renormalon prediction than the fit of Figure B.7. Data from either PVDIS or MINERVA would be useful in clarifying the picture.

B.6 Recent Progress in Higher Twist

Progress in subject of higher twist since the Jaffe and Soldate and other papers has been relatively slow until recently. One reason is the lack of reliable data; the advent of HERA and other high energy facilities has provided a solid data base from which higher twist effects can be determined. Recent experiments on the spin structure function g_2 have

also shown the effects of higher twist operators. Finally, higher twist effects have become important for the interpretation of B-meson decays.

On the theoretical side, the anomalous dimensions for the higher twist operators has not been computed. This information is needed to evolve the higher twist effects from the Q^2 values where the data is obtained to lower scales where the physics might have a more significant interpretation. At the workshop, theoretical talks discussed methods to compute the anomalous dimensions. It is quite possible that this work will be completed before our data are taken, so it will be easier to interpret.

The lattice offers the possibility of computing higher twist effects. At the workshop, we heard that the quark-quark correlations, which do not involve disconnected loops, could be relatively straightforward to compute. The quark-gluon operators are more difficult. The anomalous dimensions will be needed to evolve the lattice computations to the Q^2 values relevant to PVDIS.

B.7 Additional Hadron Physics with Deuterium

Another hadronic effect that could appear in the data is charge symmetry violation (CSV). We present what we know about CSV and then show how CSV can be distinguished from higher twist effects.

B.7.1 Charge Symmetry Violation

One critical assumption for the cancellation of the structure functions in A^{PV} for the deuteron is charge symmetry, namely $u^p = d^n$ and $u^n = d^p$. Charge symmetry violation (CSV) can be parametrized by new PDF's

$$\delta u \equiv u^p - d^n; \quad \delta d \equiv d^p - u^n; \quad R^{CSV} \equiv \frac{\delta u - \delta d}{u + v}$$

There is no direct evidence for CSV at the parton level [12]. However, our PVDIS data will be more sensitive to CSV than any previous data, so we can set the best limits at large values of x.

There is some indirect evidence for CSV in neutrino scattering [13,14]. The Paschos-Wolfenstein ratio

$$R^{PW} = \frac{\sigma\langle \nu N \to \nu X\rangle - \sigma\langle \overline{\nu} N \to \overline{\nu} X\rangle}{\sigma\langle \nu N \to \mu X\rangle - \sigma\langle \overline{\nu} N \to \overline{\mu} X\rangle} \sim \frac{1}{2} - \sin^2\theta_W$$

which has been precisely measured by the NuTeV collaboration [15], is quite sensitive to CSV. In particular,

$$\frac{\delta R^{PW}}{R^{PW}} \sim 0.85 R^{CSV}$$

The discrepancy of the NuTeV result with the Standard Model may indeed be due to CSV.

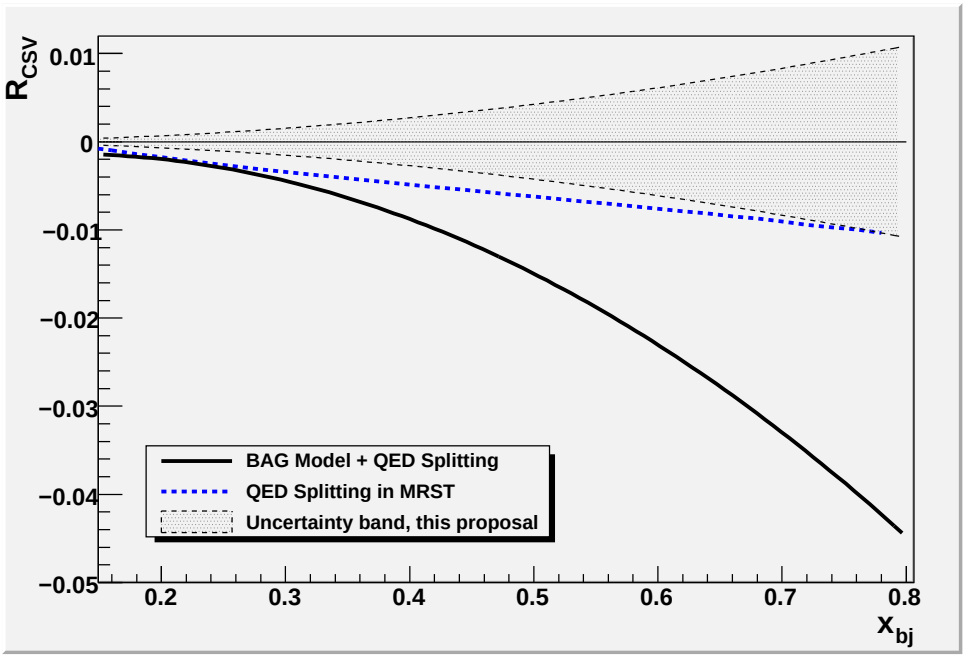

Figure B.14: Predictions of CSV versus x. The vertical axis is the fractional change in A_{PV} due to CSV. The uncertainty band is based on the fit described in Section B.7.2. The MRST results shown here account for QED splitting in the Q^2 evolution only, and do not include non-perturbative effects.

As a consequence of the above, the MRST group has added CSV-violating terms to their global fits [16] and have found that sufficient CSV is allowed to account for the NuTeV result. Non-zero values of R^{CSV} have been suggested in the literature caused both by non-perturbative QCD effects [17,18] as well as QED effects in the Q^2 evolution [19,20]. These are also in the range that would be significant for the NuTeV result.

The corrections due to CSV for A^{PV} for deuterium are

$$\frac{\delta^{CSV} a_1^D}{a_1^d} = \left(\frac{3}{10} + \frac{2C_{1u} + C_{1d}}{2(2C_{1u} - C_{1d}}\right) R^{CSV}$$

$$\frac{\delta^{CSV} a_3^D}{a_3^d} = \left(\frac{3}{10} + \frac{2C_{2u} + C_{2d}}{2(2C_{2u} - C_{2d})}\right) R^{CSV}$$

The effect of the CSV suggested in Ref. [17, 18, 19, 20] on A^{PV} is plotted in Figure B.14. The size of the CSV effect is within reach of our sensitivity. Since we can obtain high precision in several narrow bins of x for $x > 0.4$ with the JLab upgrade, we will be in an ideal position to study CSV. Moreover, the effect depends on strongly on x but is independent of y, in contrast to physics beyond the Standard Model. This signature will be a powerful method to demonstrate that CSV is indeed the explanation for any deviation from the prediction of Equation B.12.

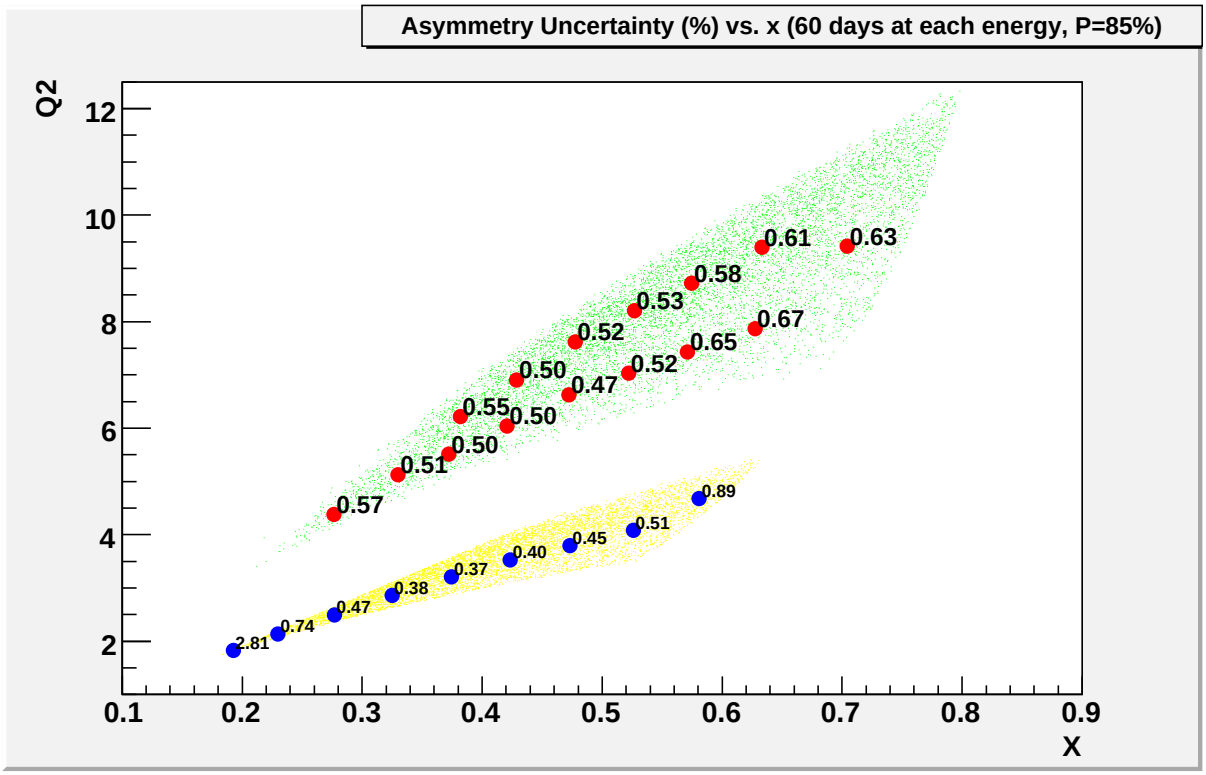

Figure B.15: Projected data with errors for the proposed experiment.

B.7.2 Fitting the PVDIS Data to Untangle the Physics

The observation of CSV is possible with our apparatus only if the effect varies with x. An x-independent CSV effect would be indistinguishable from a change in the C_1's. It is quite natural, however, to expect that the x-dependence is similar to that shown in Figure B.14, and we will make that assumption in our further discussion.

If negligible Q^2 and x dependence is observed, we will have to make plausible assumptions about the form of the possible hadronic effects in order to untangle the various effects of hadronic and electroweak physics. We plan to fit the asymmetries to the following function

$$A_{PV} = A_{PV}^{EW}\left(1 + \beta_{HT}\frac{1}{(1-x)^3 Q^2} + \beta_{CSV}x^2\right) \tag{B.18}$$

The projected data set with errors is given in Figure B.15.

The form of the higher twist function in Equation B.18 is suggested by the x dependence of the PDF's and the assumption the the higher twist observed in F_2^γ in our x range is rather flat in x. We have fit hypothetical data with the projected errors, and the resulting statistical error on the fit parameters are:

$$\delta A_{PV}^{EW}/A_{PV}^{EW} = 0.3\%; \quad \delta\beta_{HT} = 0.0026; \quad \delta\beta_{CSV} = 0.017$$

With this method, we use the full statistical power of the data set. However, the resulting errors have some sensitivity to the exact form of the chosen fitting functions. Under the

scenario where the hadronic effects are small, these errors are negligible as long as we assume that CSV and higher twist effects depend strongly on x, as expected. The one-sigma band for the CSV term is plotted in Figure B.14.

B.8 Measurement at Low y

The SOLID apparatus is designed to obtain data at large values of y where the a_3 term dominates. Data at low values of y would also be valuable in order to distinguish isolate the hadronic effects. The 11 GeV energy of JLab is a bit low for this purpose, but a point at $x \sim 0.3$ and $Q^2 \sim 1.5$ is possible with the SHMS spectrometer operating at a scattering angle of about 7°. The SOLID apparatus would contribute two more points at $x = 0.3$ but with large y, one at the Q^2 of the SHMS point and one at higher Q^2. The points at the same Q^2 but different y would directly measure the a_3 term and would thus measure the C_2's independently. The effects of CSV would cancel in this study. Comparing the points at the same x but different Q^2 would provide an independent measurement of the higher twist contribution.

B.9 Summary

The only higher twist corrections that can apply to the dominant $Y_1 a_1$ term involve the correlation between valance up and down quarks (see Section B.2.3). In other words, the term is sensitive only to di-quark terms on the OPE. This is a unique feature of PVDIS; most other experiments are also sensitive to quark-gluon correlations.

The asymmetry A^{PV} in deuterium that we plan to measure also has a 10% contribution from the $Y_3 a_3$ axial hadronic term, which does have contributions to higher twist due to quark-gluon correlations. These terms form a potential background to our extraction of quark-quark correlations. Based on existing data, these effects are at most on the order of 1% of A^{PV}, barely within our sensitivity. Several models, including the bag model and the instanton model, predict that the quark-gluon terms are an order of magnitude or so larger than the quark-quark terms. One goal of the experiment is to empirically determine whether or not this important feature of higher twist operators is true or not. If we were to observe a Q^2-dependent contribution of 5 σ or so, diquarks will be the best explanation, and they will be comparable to the quark-gluon contributions.

Future neutrino experiments such as MINERVA may provide a more precise measurement of the higher twist contribution to F_3. That will enable us to remove the higher twist contribution in the $Y_3 a_3$ term and improve the sensitivity of our search for quark-quark correlations.

The possibility that $R^\gamma \neq R^{\gamma Z}$ was eliminated, both by the CVC nature of the currents and by the fact that the ratio is flavor blind for the deuteron (see Section B.2.4). Target mass corrections (see Section B.3.2) were also found to introduce no uncertainty if consistent procedures are used with the PDF's.

B.10 Conclusions

At the workshop, we reached three main conclusions:

1. The contribution of higher twist to the a_3 term can be estimated to sufficient precision by using existing neutrino data, which hopefully will be augmented by MINERVA data. The higher twist contribution to the a_1 term, which must be due to quark-quark correlations, will be extracted from the data by using a plausible fitting function as described in Section B.7.2. With this procedure, the presence of higher twist contributions to A^{PV} will not significantly degrade the measurement of the $C_2's$ as a search for new physics.

2. If we do observe a large Q^2 dependence in A_{PV} that are bigger than the possible contributions from just the axial-hadronic part of the asymmetry, this will provide a clean signature for the presence of quark-quark correlations in the nucleon. Such an observation would be very exciting, and the possibility merits that the physics of higher twist be included as a bullet in the abstract of the SOLID proposal.

3. Recent theoretical developments, especially the development of techniques that have the potential to compute the anomalous dimensions for higher twist, will be important for evaluating the physical significance of our data.

Bibliography

[1] SoLID Collaboration, " Precision Measurement of Parity-violation in Deep Inelastic Scattering Over a Broad Kinematic Range," 2009. URL http://www.jlab.org/exp_prog/proposals/09/PR-09-012.pdf. Proposal to JLab PAC34.

[2] T. Hobbs and W. Melnitchouk, "Finite-Q^2 corrections to parity-violating DIS," *Phys. Rev.*, vol. D77, p. 114023, 2008, 0801.4791.

[3] C. Y. Prescott *et al.*, "Parity non-conservation in inelastic electron scattering," *Phys. Lett.*, vol. B77, pp. 347–352, 1978.

[4] C. Y. Prescott *et al.*, "Further Measurements of Parity Nonconservation in Inelastic electron Scattering," *Phys. Lett.*, vol. B84, p. 524, 1979.

[5] P. A. Souder *et al.*, "Measurement of parity violation in the elastic scattering of polarized electrons from C-12," *Phys. Rev. Lett.*, vol. 65, pp. 694–697, 1990.

[6] P. L. Anthony *et al.*, "Precision measurement of the weak mixing angle in Moeller scattering," *Phys. Rev. Lett.*, vol. 95, p. 081601, 2005, hep-ex/0504049.

[7] S.-L. Zhu, S. J. Puglia, B. R. Holstein, and M. J. Ramsey-Musolf, "The nucleon anapole moment and parity-violating e p scattering," *Phys. Rev.*, vol. D62, p. 033008, 2000, hep-ph/0002252.

[8] R. D. Young, J. Roche, R. D. Carlini, and A. W. Thomas, "Extracting nucleon strange and anapole form factors from world data," *Phys. Rev. Lett.*, vol. 97, p. 102002, 2006, nucl-ex/0604010.

[9] X. C. Zheng, "Disparity e08-011." URL http://hallaweb.jlab.org/experiment/E05-007/.

[10] M. J. Ramsey-Musolf and S. Su, "Low energy precision test of supersymmetry," *Phys. Rept.*, vol. 456, pp. 1–88, 2008, hep-ph/0612057.

[11] A. Kurylov, M. J. Ramsey-Musolf, and S. Su, "Supersymmetric effects in parity-violating deep inelastic electron nucleus scattering," *Phys. Lett.*, vol. B582, pp. 222–228, 2004, hep-ph/0307270.

[12] J. T. Londergan and A. W. Thomas, "The validity of charge symmetry for parton distributions," *Prog. Part. Nucl. Phys.*, vol. 41, pp. 49–124, 1998, hep-ph/9806510.

[13] J. T. Londergan and A. W. Thomas, "Charge symmetry violation corrections to determination of the Weinberg angle in neutrino reactions," *Phys. Rev.*, vol. D67, p. 111901, 2003, hep-ph/0303155.

[14] J. T. Londergan and A. W. Thomas, "Charge symmetry violating contributions to neutrino reactions," *Phys. Lett.*, vol. B558, pp. 132–140, 2003, hep-ph/0301147.

[15] G. P. Zeller *et al.*, "A precise determination of electroweak parameters in neutrino nucleon scattering," *Phys. Rev. Lett.*, vol. 88, p. 091802, 2002, hep-ex/0110059. [Erratum-ibid. **90**, 239902 (2003)].

[16] A. D. Martin, R. G. Roberts, W. J. Stirling, and R. S. Thorne, "Uncertainties of predictions from parton distributions. II: Theoretical errors," *Eur. Phys. J.*, vol. C35, pp. 325–348, 2004, hep-ph/0308087.

[17] E. Sather, "Isospin violating quark distributions in the nucleon," *Phys. Lett.*, vol. B274, pp. 433–438, 1992.

[18] E. N. Rodionov, A. W. Thomas, and J. T. Londergan, "Charge asymmetry of parton distributions," *Mod. Phys. Lett.*, vol. A9, pp. 1799–1806, 1994.

[19] A. D. Martin, R. G. Roberts, W. J. Stirling, and R. S. Thorne, "Parton distributions incorporating QED contributions," *Eur. Phys. J.*, vol. C39, pp. 155–161, 2005, hep-ph/0411040.

[20] M. Gluck, P. Jimenez-Delgado, and E. Reya, "Radiatively generated isospin violations in the nucleon and the NuTeV anomaly," *Phys. Rev. Lett.*, vol. 95, p. 022002, 2005, hep-ph/0503103.

[21] J. T. Londergan, D. P. Murdock, and A. W. Thomas, "Parton charge symmetry violation: Electromagnetic effects and W production asymmetries," *Phys. Rev.*, vol. D73, p. 076004, 2006, hep-ph/0603208.

[22] J. T. Londergan, D. P. Murdock, and A. W. Thomas, "Experimental tests of charge symmetry violation in parton distributions," *Phys. Rev.*, vol. D72, p. 036010, 2005, hep-ph/0507029.

[23] J. T. Londergan and A. W. Thomas, "Implications of current constraints on parton charge symmetry," *J. Phys.*, vol. G31, pp. 1151–1163, 2005.

[24] J. D. Bjorken, "Model independent remarks on electron - quark parity violating neutral - current couplings," *Phys. Rev.*, vol. D18, p. 3239, 1978.

[25] L. Wolfenstein, "Testing the Weinberg-Salam model in polarized e d and e p deep inelastic scattering," *Nucl. Phys.*, vol. B146, p. 477, 1978.

[26] E. Derman, "Parity violation in polarized electron - deuteron scattering without the parton model," *Phys. Rev.*, vol. D19, p. 133, 1979.

[27] S. J. Brodsky, "Dynamical higher-twist and high x phenomena: A window to quark quark correlations in QCD," 2000, hep-ph/0006310.

[28] R. L. Jaffe and M. Soldate, "Twist Four in the QCD Analysis of Leptoproduction," *Phys. Lett.*, vol. B105, pp. 467–472, 1981.

[29] R. L. Jaffe and M. Soldate, "Twist Four in Electroproduction: Canonical Operators and Coefficient Functions," *Phys. Rev.*, vol. D26, pp. 49–68, 1982.

[30] P. Castorina and P. J. Mulders, "Twist four corrections to asymmetry in polarized electron Deuteron scattering," *Phys. Rev.*, vol. D31, pp. 2760–2764, 1985.

[31] G. F. Sacco, "Hadronic Effects in Parity Violating Electron Scattering," 2009, 0902.1285.

[32] M. Amarian *et al.*, "Q^2 evolution of the neutron spin structure moments using a He-3 target," *Phys. Rev. Lett.*, vol. 92, p. 022301, 2004, hep-ex/0310003.

[33] Z. E. Meziani *et al.*, "Higher twists and color polarizabilities in the neutron," *Phys. Lett.*, vol. B613, pp. 148–153, 2005, hep-ph/0404066.

[34] A. Deur, "Higher-twist analysis of moments of spin structure function," 2005, nucl-ex/0508022.

[35] A. Deur *et al.*, "Experimental determination of the evolution of the Bjorken integral at low Q^2," *Phys. Rev. Lett.*, vol. 93, p. 212001, 2004, hep-ex/0407007.

[36] S. Alekhin, S. A. Kulagin, and R. Petti, "Modeling Lepton-Nucleon Inelastic Scattering from High to Low Momentum Transfer," *AIP Conf. Proc.*, vol. 967, pp. 215–224, 2007, 0710.0124.

[37] M. Virchaux and A. Milsztajn, "A Measurement of α_s and higher twists from a QCD analysis of high statistics F-2 data on hydrogen and deuterium targets," *Phys. Lett.*, vol. B274, pp. 221–229, 1992.

[38] P. Amaudruz *et al.*, "The ratio $F_2(n)$ / $F_2(p)$ in deep inelastic muon scattering," *Nucl. Phys.*, vol. B371, pp. 3–31, 1992.

[39] J. Blumlein and H. Bottcher, "Higher Twist Contributions to the Structure Functions $F_2^p(x,Q^2)$ and $F_2^d(x,Q^2)$ at Large x and Higher Orders," *Phys. Lett.*, vol. B662, pp. 336–340, 2008, 0802.0408.

[40] "MINERvA Technical Design Report," FERMILAB-DESIGN-2006-01.

[41] W. Melnitchouk, I. R. Afnan, F. R. P. Bissey, and A. W. Thomas, "Comment on 'Parton distributions, d/u, and higher twist effects at high x'," *Phys. Rev. Lett.*, vol. 84, p. 5455, 2000, hep-ex/9912001.

[42] W. Melnitchouk and A. W. Thomas, "Neutron / proton structure function ratio at large x," *Phys. Lett.*, vol. B377, pp. 11–17, 1996, nucl-th/9602038.

[43] S. I. Alekhin, "Global fit to the charged leptons DIS data: α_s, parton distributions, and high twists," *Phys. Rev.*, vol. D63, p. 094022, 2001, hep-ph/0011002.

[44] S. Kuhlmann *et al.*, "Large-x parton distributions," *Phys. Lett.*, vol. B476, pp. 291–296, 2000, hep-ph/9912283.

[45] S. Bultmann, "The BoNuS experiment at Jefferson Lab," *AIP Conf. Proc.*, vol. 747, pp. 46–49, 2005.

[46] I. Cloet, W. Bentz, and A. W. Thomas. private communication.

[47] PAC34, " PAC34 Report ," 2009. URL http://www.jlab.org/exp_prog/PACpage/PAC34/PAC34_report.pdf.

[48] L. W. Mo and Y.-S. Tsai, "Radiative corrections to elastic and inelastic e p and mu p scattering," *Rev. Mod. Phys.*, vol. 41, pp. 205–235, 1969.

[49] W. J. Marciano and A. Sirlin, "On Some General Properties of the O(α) Corrections to Parity Violation in Atoms," *Phys. Rev.*, vol. D29, p. 75, 1984.

[50] K. Hagiwara *et al.*, "Review of particle physics," *Phys. Rev.*, vol. D66, p. 010001, 2002.

[51] S. Eidelman *et al.*, "Review of particle physics," *Phys. Lett.*, vol. B592, p. 1, 2004.

[52] E. V. Shuryak and A. I. Vainshtein, "Theory of Power Corrections to Deep Inelastic Scattering in Quantum Chromodynamics. 2. Q^4 Effects: Polarized Target," *Nucl. Phys.*, vol. B201, p. 141, 1982.

[53] E. V. Shuryak and A. I. Vainshtein, "Theory of Power Corrections to Deep Inelastic Scattering in Quantum Chromodynamics. 1. Q^2 Effects," *Nucl. Phys.*, vol. B199, p. 451, 1982.

[54] J. Blumlein, H. Bottcher, and A. Guffanti, "Non-singlet QCD analysis of deep inelastic world data at O(α_s^2)," *Nucl. Phys.*, vol. B774, pp. 182–207, 2007, hep-ph/0607200.

[55] P. Castorina and P. J. Mulders, "TWIST FOUR CORRECTIONS TO CHARGED AND NEUTRAL CURRENT NEUTRINO SCATTERING," *Phys. Rev.*, vol. D31, p. 2753, 1985.

[56] S. Fajfer and R. J. Oakes, "Twist - Four Effects on the Asymmetry in Polarized Electron Deuteron Scattering and $\sin^2\theta_W$," *Phys. Rev.*, vol. D30, p. 1585, 1984.

[57] A. V. Sidorov and C. Weiss, "Higher twists in polarized DIS and the size of the constituent quark," *Phys. Rev.*, vol. D73, p. 074016, 2006, hep-ph/0602142.

[58] B. Dressler, K. Goeke, M. V. Polyakov, and C. Weiss, "Flavor asymmetry of polarized antiquark distributions and semi-inclusive DIS," *Eur. Phys. J.*, vol. C14, pp. 147–157, 2000, hep-ph/9909541.

[59] J. Balla, M. V. Polyakov, and C. Weiss, "Nucleon matrix elements of higher-twist operators from the instanton vacuum," *Nucl. Phys.*, vol. B510, pp. 327–364, 1998, hep-ph/9707515.

[60] E. Stein, M. Maul, L. Mankiewicz, and A. Schafer, "Renormalon model predictions for power-corrections to flavour singlet deep inelastic structure functions," *Nucl. Phys.*, vol. B536, pp. 318–342, 1998, hep-ph/9803342.